

# A three-dimensional dynamic analysis scheme for the interaction between trains and curved railway bridges



Elias G. Dimitrakopoulos\*, Qing Zeng

Department of Civil and Environmental Engineering, The Hong Kong University of Science and Technology, Clear Water Bay, Kowloon, Hong Kong<sup>1</sup>

## ARTICLE INFO

### Article history:

Received 9 November 2013

Accepted 1 December 2014

### Keywords:

Vehicle–bridge interaction

High-speed railway bridge

Curved bridge

Concrete bridge

## ABSTRACT

The present paper proposes an original scheme for the dynamic analysis of the vehicle–bridge interaction (VBI) between trains and curved in-plan bridges. Key features are the three-dimensional vehicle dynamics formulation, and the matrix statement of the equations which condense the VBI dynamics, making the scheme generic. The analysis brings forward the interaction along the radial and torsional sense of curved bridges, which are often neglected for straight bridges. Specifically, the study shows that the (centrifugal and Coriolis) forces generated due to the curved path govern the lateral dynamics of the vehicle–bridge system when the curvature and/or the velocity are high.

© 2014 Elsevier Ltd. All rights reserved.

## 1. Introduction

Railway networks are expanding worldwide, and especially in China, to meet the increasing requirements for high-standard transportation. After ten years of constructing new high-speed railways and upgrading existing conventional railway lines, China now shares the world's longest (Fig. 1 [1]) high-speed railway (HSR). Compared with the conventional railway lines, HSRs have a higher percentage of bridges [2], mainly for reasons of safety, comfort and mitigation of noise pollution. For instance, the Beijing–Shanghai HSR line is 1318 km long, out of which 1059.4 km (80.5% of the whole line [3]) is on mostly viaduct bridges. Further, the operational speed for HSR trains in China has been limited from 350 km/h (in 2011) to 300 km/h [4] (in 2013). These unprecedented speeds trains operate, over an ever increasing length of railway bridges, create incentive to revisit their dynamic interaction to ensure safety and comfort during travel.

The VBI dynamics attracts the attention of researchers for almost a century [5]. As the field matured, the standard VBI model shifted, from the moving-force model [6–10], to the moving-mass model [11–14] and then to the sprung mass model [15–18]. Au et al. [16] compared the influence of five different vehicle models, on a cable-stayed bridge, and noted that the moving force and the moving mass models tend to underestimate the impact effect. During the last decades, the advent of personalized, high computational power enabled the consideration of more sophisticated

models, for both bridges and vehicles. Most recent studies, e.g. [3,19–32], simulate the vehicle as an assembly of rigid-bodies (car body, bogies and wheelsets) connected with springs and dashpots representing the properties of the suspension system. For the purpose of a numerical VBI analysis, the response of bridges is captured either with integration in the time domain of the complete geometrical model [10,23,33–36] or with the modal superposition method [9,21,37–42]. Alternatively, the so-called VBI-element can be used which condenses (dynamically) the vehicle and the bridge subsystems (Yang and Lin [33]). Yang and Yau [34] refined the VBI-element approach taking into account the pitching effect of the vehicle, while Lou and Zeng [36] proposed a similar element considering a four-axle 10-DOF vehicle model with two-layer suspension systems. Very recently, Neves et al. [43] proposed a direct-method for the analysis of the nonlinear VBI along the vertical direction.

The majority of the VBI studies examine the problem solely in the vertical direction. Hence, despite the abundance of VBI studies, to the authors' knowledge, studies on the VBI of curved in-plan bridges (e.g. Fig. 2 [44]) are scarce. In particular, Yang et al. [45] derived closed-form solutions for a single-span, simply supported, horizontally curved beam subjected to pairs of moving vertical and horizontal (centrifugal) loads. Xia et al. [41] examined the lateral VBI dynamics of a 3D train model running on curved railway lines, supported on straight girders. Following a different approach than the one proposed herein, that study [41] concluded that in curved bridges, the centrifugal forces dominate the lateral dynamics, even over the effect of the hunting motion of the wheelset. The study further argued that no resonance is observed in the lateral VBI in

<sup>1</sup> <http://www.ce.ust.hk/>.

\* Corresponding author. Tel.: +852 2358 5975.

E-mail addresses: [ilias@ust.hk](mailto:ilias@ust.hk) (E.G. Dimitrakopoulos), [qzeng@ust.hk](mailto:qzeng@ust.hk) (Q. Zeng).

curved bridges [41], and compared their numerical results with field experiments.

The primary motivation for this study is: (i) the expanding conventional and HSR networks worldwide, (ii) the ever increasing ratio of bridges comprising contemporary HSR lines, (iii) the unprecedented speeds trains operate, and (iv) the lack of published research on the dynamic VBI in the case of curved in-plan bridges. The present research deploys an original and versatile framework, for the simulation of the interaction dynamics between trains and curved, in-plan, railway bridges (Fig. 2).

## 2. Proposed approach

With the aim to avoid an ad hoc treatment of the VBI problem, the proposed approach deploys a matrix formulation, and results in a set of equations of motion (Eq. (23)) which are condensed and easily reproducible. For a different bridge and/or different vehicle-models or numbers of vehicles, one has only to implement the same matrix equations, presented later in Eq. (23), for the pertinent matrices.

The examined dynamical system consists of the vehicle subsystem and the bridge subsystem. The two subsystems are coupled through the contact forces between the vehicle wheels and the rails. The study simulates the, straight or curved in-plan (horizontally), bridges with the finite element method (FEM), and models the vehicles as multibody assemblies. The solution of the global equations provides the response of both the bridge and the vehicle simultaneously. The mass matrix, the stiffness matrix, the damping matrix and the loading vector of the global (coupled vehicle-bridge) system become time-dependent. The paper accounts for the self-excitations, such as the elevation and alignment rail irregularities, the hunting motion of the wheelset, and the subsequent rolling rotation due to the conicity of the wheels. The study also considers the track eccentricity (offset) with respect to the shear center of the deck's section and the effect of the cant angle. It is assumed that all deformations remain small and that the linear elastic theory applies. Numerically, the proposed framework is realized with MATLAB [46].



Fig. 2. A continuous curved in-plan railway bridge of the Lan-wu line, in China. (Image CC from CRCC [44]).

### 2.1. Vehicle modeling

The train vehicles are modeled as multibody assemblies comprised of (Fig. 3(a)): (i) one car body, (ii) two bogies and (iii) four wheelsets of each vehicle, which are all considered as rigid bodies. Fig. 3(a) presents the typical, 27 degrees of freedom (DOF's), 3D vehicle model [45] utilized in this study. The car body, the front and the rear bogies are assigned five DOF's each: the vertical and the lateral displacements, the yawing, the rolling, and the pitching rotations (Fig. 3(b)). For each wheelset, only three DOF's are designated: the vertical and the lateral displacements, and the rolling rotation.

Following [47], the study employs three systems of reference to formulate the equations of motion of the vehicle: an inertia (space-fixed) system  $O-XYZ$ , a moving trajectory system  $O'-X^{ti}Y^{ti}Z^{ti}$ , and a body-fixed system  $O^{ir}-X^{ir}Y^{ir}Z^{ir}$  (Fig. 4).

The definition of the moving trajectory system  $O'-X^{ti}Y^{ti}Z^{ti}$  requires only a time-dependent coordinate, the arc length,  $s^i$  (Fig. 4). The orientation of the trajectory system is then defined using three Euler angles:  $\psi^{ti}$  (yawing),  $\phi^{ti}$  (rolling) and  $\theta^{ti}$  (pitching)

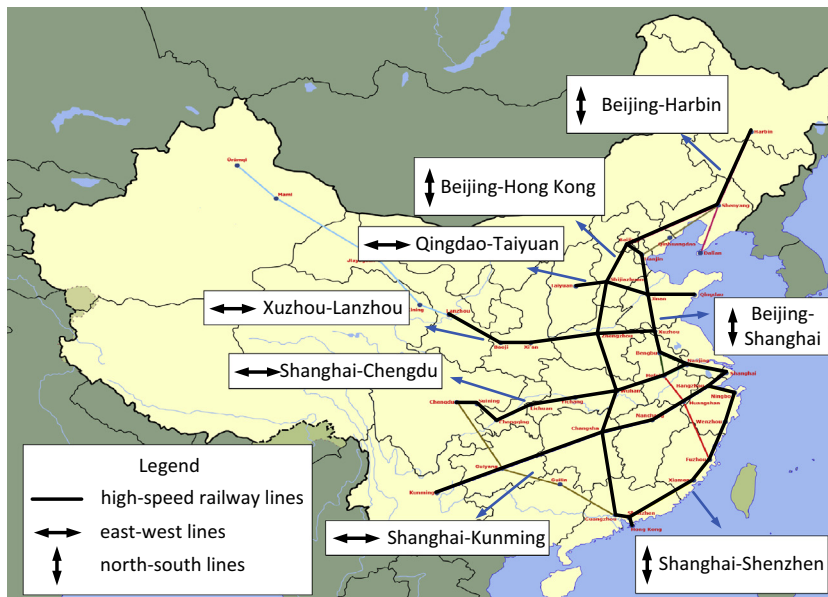


Fig. 1. The blue print of the planned high-speed railway network in China for 2020. The total envisaged length for 2020 is 50,000 km. (Image CC from Alancrh [1]).

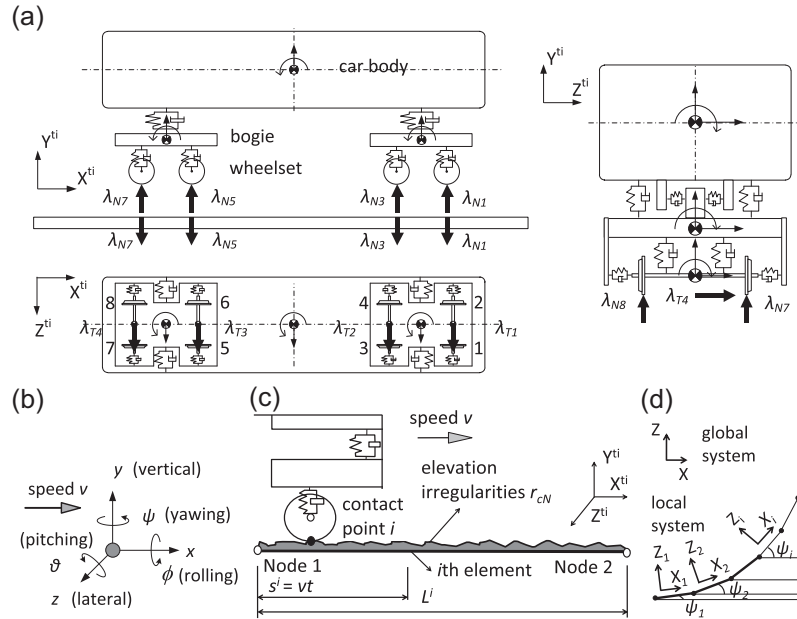


Fig. 3. (a) The adopted vehicle model and the contact forces  $\lambda_N, \lambda_T$  considered, (b) sign convention of the vehicle, (c) a beam element in contact with the wheel and (d) local and global coordinate systems of a curved beam.

about the three axes  $Y^{ti}, X^{ti}$  and  $Z^{ti}$  respectively (Fig. 4 [47]). All three Euler angles are known functions of the arc length  $s^i$ . The longitudinal direction of the trajectory system  $O'X^{ti}$  is set tangent to the curve at its origin  $O'$  (Fig. 4).

The body-fixed system  $O^{ir}-X^{ir}Y^{ir}Z^{ir}$  follows the longitudinal-tangential to the trajectory-motion of the trajectory system, with its origin fixed to the center of mass of the body. The motion of the rigid body in the trajectory coordinate system is described with five time-dependent coordinates: two translations  $y^{ir}$  (vertical) and  $z^{ir}$  (lateral), and three rotations  $\psi^{ir}$  (yawing),  $\phi^{ir}$  (rolling) and  $\theta^{ir}$  (pitching) about the three axes  $Y^{ir}, X^{ir}$  and  $Z^{ir}$  respectively (Fig. 4).

The Newton–Euler equation of motion can describe the motion of the vehicle in terms of generalized trajectory coordinates as [47]:

$$\mathbf{M}^V(t)\ddot{\mathbf{u}}^V = \mathbf{F}_e^V + \mathbf{F}_v^V(t) \quad (1)$$

where superscript  $( )^V$  denotes the vehicle subsystem and  $\ddot{\mathbf{u}}^V$  is the generalized acceleration vector in the trajectory system. Throughout this paper the upper-dot denotes the time derivative. The displacement vector of a single vehicle with 27 DOF's is:

$$\begin{cases} \mathbf{u}^V = [\mathbf{u}^c \ \mathbf{u}^{t1} \ \mathbf{u}^{t2} \ \mathbf{u}^{w1} \ \mathbf{u}^{w2} \ \mathbf{u}^{w3} \ \mathbf{u}^{w4}]^T \\ \mathbf{u}^c = [y^c \ z^c \ \psi^c \ \phi^c \ \theta^c] \\ \mathbf{u}^t = [y^t \ z^t \ \psi^t \ \phi^t \ \theta^t] \\ \mathbf{u}^w = [y^w \ z^w \ \phi^w] \end{cases} \quad (2)$$

where the superscripts  $c, t, w$  denote the car body, the bogies and the wheelsets respectively.  $y$  and  $z$  denote the vertical and lateral displacement;  $\psi, \phi$  and  $\theta$  are, the yawing, rolling and pitching rotations (Fig. 3(b)).  $\mathbf{M}^V(t)$  is the mass matrix;  $\mathbf{F}_e^V$  is the vector of external forces;  $\mathbf{F}_v^V(t)$  is the vector of centrifugal forces and Coriolis forces - the first and the second item in Eq. (3).

To illustrate the details of Eq. (1), consider a specific rigid body component of the vehicle, for instance the car-body (indicated with superscript  $c$ ). It holds [47]:

$$\begin{cases} \mathbf{M}^c(t) = m^c \mathbf{L}^c(t)^T \mathbf{L}^c(t) + \bar{\mathbf{H}}^c(t)^T \bar{\mathbf{I}}_{\theta\theta}^c \bar{\mathbf{H}}^c(t) \\ \mathbf{F}_e^c = \mathbf{F}_G^c - \mathbf{F}_K^c - \mathbf{F}_D^c \\ \mathbf{F}_v^c(t) = -m^c \mathbf{L}^c(t)^T \gamma_R^c - \bar{\mathbf{H}}^c(t)^T \{ \bar{\mathbf{I}}_{\theta\theta}^c \bar{\gamma}_\alpha^c + \bar{\omega}^c \times (\bar{\mathbf{I}}_{\theta\theta}^c \bar{\omega}^c) \} \end{cases} \quad (3)$$

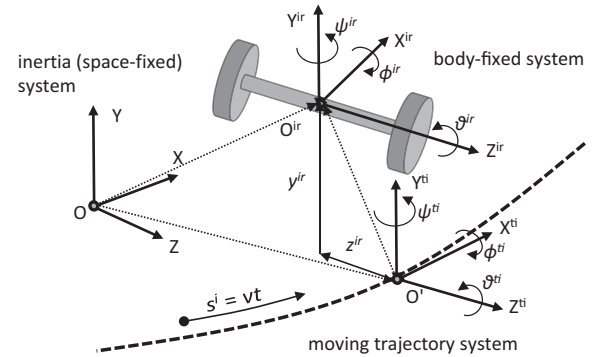


Fig. 4. The three coordinate systems used, adapted from [47].

Throughout this paper superscript T denotes the transpose of a matrix and the upper-bar symbol,  $\bar{(\ )}$ , indicates that the particular quantity is defined in the body-fixed system.  $\bar{\omega}$  is the angular velocity vector,  $m$  is the mass and  $\bar{\mathbf{I}}_{\theta\theta}$  is the inertia tensor (defined in the body-fixed system) about the principle axes of each rigid body. For the car body we have:

$$\bar{\mathbf{I}}_{\theta\theta}^c = \text{diag} [ I_{xx}^c \ I_{yy}^c \ I_{zz}^c ] \quad (4)$$

$\mathbf{L}$  and  $\bar{\mathbf{H}}$  are velocity transformation matrices, corresponding to the translational and rotational DOF's according to [47]. In the case of curved bridges, both  $\mathbf{L}$  and  $\bar{\mathbf{H}}$  are varying in time.  $\mathbf{F}_G$  is the gravity force vector;  $\mathbf{F}_K$  is the vector of the elastic forces;  $\mathbf{F}_D$  the vector of the damping forces.  $\gamma_R$  and  $\bar{\gamma}_\alpha$  are vectors containing the additional quadratic velocity terms produced during the time-differentiation of the absolute linear velocity and the absolute angular velocity vectors [47], respectively.

The equations for the remaining components of the vehicle, bogies and wheelsets are similar to Eq. (3). Gathering the equations of all rigid body components (car body, bogies and wheelsets) together, and replacing the elastic force vector  $\mathbf{F}_K^c$  and the damping force vector  $\mathbf{F}_D^c$  from Eq. (3) with their matrix expressions, the equation of motion for the vehicle subsystem (Fig. 3(a)) can be written as:

$$\mathbf{M}^V(t)\ddot{\mathbf{u}}^V + \mathbf{C}^V\dot{\mathbf{u}}^V + \mathbf{K}^V\mathbf{u}^V - \mathbf{W}_N^V\lambda_N - \mathbf{W}_T^V\lambda_T = \mathbf{F}^V(t) \quad (5)$$

$\mathbf{K}^V$  and  $\mathbf{C}^V$  are the stiffness and the damping matrix of the vehicle (Fig. 3(a)) given in [45].  $\mathbf{u}^V \in \mathbb{R}^{27,1}$  is the displacement vector of the vehicle given in Eq. (2) and  $\mathbf{F}^V$  is the force vector:

$$\mathbf{F}^V = \mathbf{F}_G^V + \mathbf{F}_v^V \quad (6)$$

$\lambda_N$  and  $\lambda_T$  are the normal and the tangential contact force vectors (discussed in Section 2.3) respectively, and  $\mathbf{W}_N^V$  and  $\mathbf{W}_T^V$  are the direction matrices of the corresponding contact forces  $\lambda_N$  and  $\lambda_T$ :

$$\mathbf{W}_N^V = \begin{bmatrix} \mathbf{0}_{N}^{Vu} \\ \mathbf{W}_N^{Vw} \end{bmatrix}, \quad \mathbf{W}_T^V = \begin{bmatrix} \mathbf{0}_T^{Vu} \\ \mathbf{W}_T^{Vw} \end{bmatrix} \quad (7)$$

Throughout this paper, the subscripts  $N$  and  $T$  stand for the normal and the tangential direction of contact respectively. The only non-zero entries in matrices  $\mathbf{W}_N^V$  and  $\mathbf{W}_T^V$  correspond to the wheels of the vehicle (superscript  $(\cdot)^{Vw}$ ). For the upper part of the vehicle, i.e. the car body and the bogies, (superscript  $(\cdot)^{Vu}$ ), the pertinent sub-matrices  $\mathbf{0}_N^{Vu}$  and  $\mathbf{0}_T^{Vu}$  are zero. For a single vehicle (like the one in Fig. 3(a)), it holds:  $\mathbf{0}_N^{Vu} \in \mathbb{R}^{15,8}$  and  $\mathbf{0}_T^{Vu} \in \mathbb{R}^{15,4}$ ,  $\mathbf{W}_N^{Vw} \in \mathbb{R}^{12,8}$  and  $\mathbf{W}_T^{Vw} \in \mathbb{R}^{12,4}$ ,  $\lambda_N \in \mathbb{R}^{8,1}$  and  $\lambda_T \in \mathbb{R}^{4,1}$ , where nomenclature  $\mathbf{W}_T^{Vw} \in \mathbb{R}^{12,4}$  means  $\mathbf{W}_T^{Vw}$  is a real matrix with 12 rows and 4 columns. For a single wheelset, the sub matrices  $\mathbf{W}_N^{Vwi}$  and  $\mathbf{W}_T^{Vwi}$  in Eq. (7) are:

$$\mathbf{W}_N^{Vwi} = \begin{bmatrix} 1 & 1 \\ 0 & 0 \\ -l_a & l_a \end{bmatrix}, \quad \mathbf{W}_T^{Vwi} = \begin{bmatrix} 0 \\ 1 \\ -r_w \end{bmatrix} \quad (8)$$

where  $i = 1-4$  corresponds to the four wheelsets,  $l_a$  is the half-gauge and  $r_w$  is the radius of the wheel.

## 2.2. Bridge modeling

The bridge is modeled with (3D) Euler–Bernoulli beam elements, using linear and cubic (Hermitian) shape functions [49]. Six DOF's are considered per node: three displacements and three rotations with respect to the  $X$ ,  $Y$  and  $Z$  axis accordingly.

After assembly and transformation into the global system, the mass matrix  $\mathbf{M}^B$  and the stiffness matrix  $\mathbf{K}^B$  for the entire bridge are obtained.  $\mathbf{C}^B$  is a Rayleigh damping matrix and it is calculated assuming the damping ratio of the first two modes is 0.02 [50]. The equation of motion for the bridge can be written as:

$$\mathbf{M}^B\ddot{\mathbf{u}}^B + \mathbf{C}^B\dot{\mathbf{u}}^B + \mathbf{K}^B\mathbf{u}^B + \mathbf{W}_N^B\lambda_N + \mathbf{W}_T^B\lambda_T = \mathbf{F}^B \quad (9)$$

where  $\mathbf{u}^B$  is the bridge displacement vector and  $\mathbf{F}^B$  is the vector of the loads acting on the bridge.  $\mathbf{W}_N^B$  and  $\mathbf{W}_T^B$  are the direction matrices of the contact forces for the bridge subsystem. They contain the linear shape functions for the axial and torsional DOF's and the cubic (Hermitian) shape functions for the flexural DOF's (see Eq. (17)). Again, the only nonzero entries in the  $\mathbf{W}_N^B$  and  $\mathbf{W}_T^B$  matrices correspond to the DOF's of the bridge elements (i.e. the corresponding part of the rails) in contact with the wheels of the vehicle (Fig. 3(c)).

## 2.3. Vehicle–bridge interaction

The equation of motion of the coupled vehicle–bridge system can be written as:

$$\mathbf{M}\ddot{\mathbf{u}} + \mathbf{C}\dot{\mathbf{u}} + \mathbf{K}\mathbf{u} - \mathbf{W}\lambda = \mathbf{F} \quad (10)$$

where the global mass matrix  $\mathbf{M}$ , the global stiffness matrix  $\mathbf{K}$  and the global damping matrix  $\mathbf{C}$  are created by gathering the pertinent matrices of the two individual subsystems as:

$$\mathbf{M} = \begin{bmatrix} \mathbf{M}^V(t) & \mathbf{0} \\ \mathbf{0} & \mathbf{M}^B \end{bmatrix}, \quad \mathbf{C} = \begin{bmatrix} \mathbf{C}^V & \mathbf{0} \\ \mathbf{0} & \mathbf{C}^B \end{bmatrix}, \quad \mathbf{K} = \begin{bmatrix} \mathbf{K}^V & \mathbf{0} \\ \mathbf{0} & \mathbf{K}^B \end{bmatrix} \quad (11)$$

The direction matrices  $\mathbf{W}_N$  and  $\mathbf{W}_T$ , the displacement vector  $\mathbf{u}$  and the force vector  $\mathbf{F}$  for the whole system are constructed in an analogous manner:

$$\begin{cases} \mathbf{u} = \begin{bmatrix} \mathbf{u}^V \\ \mathbf{u}^B \end{bmatrix}, \mathbf{F}(t) = \begin{bmatrix} \mathbf{F}^V(t) \\ \mathbf{F}^B \end{bmatrix}, \lambda = \begin{bmatrix} \lambda_N \\ \lambda_T \end{bmatrix}, \\ \mathbf{W} = [\mathbf{W}_N \quad \mathbf{W}_T], \mathbf{W}_N = \begin{bmatrix} \mathbf{W}_N^V \\ -\mathbf{W}_N^B \end{bmatrix}, \mathbf{W}_T = \begin{bmatrix} \mathbf{W}_T^V \\ -\mathbf{W}_T^B \end{bmatrix} \end{cases} \quad (12)$$

The scheme is readily applicable for different bridge and vehicle models, or numbers of vehicles, by adjusting the pertinent matrices in Eq. (12). For example:

- For a single vehicle with  $nV$  DOF's (e.g.  $nV = 27$ ) and 8 wheels, and a bridge system with  $nB$  DOF's, it holds:

$$\begin{aligned} \mathbf{M}, \mathbf{C}, \mathbf{K} &\in \mathbb{R}^{nV+nB, nV+nB}, \quad \mathbf{u}, \mathbf{F} \in \mathbb{R}^{nV+nB, 1} \\ \mathbf{W}_N &\in \mathbb{R}^{nV+nB, 8}, \quad \mathbf{W}_T \in \mathbb{R}^{nV+nB, 4}, \quad \lambda_N \in \mathbb{R}^{8, 1}, \quad \lambda_T \in \mathbb{R}^{4, 1} \end{aligned} \quad (13)$$

where again,  $\mathbf{W}_T \in \mathbb{R}^{nV+nB, 4}$  for instance, indicates that matrix  $\mathbf{W}_T$  is a real matrix with  $(nV + nB)$  rows and four columns.

- Similarly, for  $\kappa$  identical vehicles with  $nV$  DOF's each, it holds:

$$\begin{aligned} \mathbf{M}, \mathbf{C}, \mathbf{K} &\in \mathbb{R}^{\kappa \times nV + nB, \kappa \times nV + nB}, \quad \mathbf{u}, \mathbf{F} \in \mathbb{R}^{\kappa \times nV + nB, 1} \\ \mathbf{W}_N &\in \mathbb{R}^{\kappa \times nV + nB, \kappa \times 8}, \quad \mathbf{W}_T \in \mathbb{R}^{\kappa \times nV + nB, \kappa \times 4}, \\ \lambda_N &\in \mathbb{R}^{\kappa \times 8, 1}, \quad \lambda_T \in \mathbb{R}^{\kappa \times 4, 1} \end{aligned} \quad (14)$$

While the train is moving over the bridge, the contact forces change with respect to both time ( $t$ ) and space ( $s^i$ ). The contact forces  $\lambda_N$  and  $\lambda_T$  between the wheels and the bridge (Fig. 3(a)) couple in Eq. (10) the two sets of equations, Eqs. (5) and (9), describing the response of the two subsystems. In particular, the location of the contact point  $i$  (Fig. 3(c)), for a vehicle with constant speed  $v$  is  $s^i = vt$  and thus, the direction sub-matrices  $\mathbf{W}_N^B$  and  $\mathbf{W}_T^B$  (the shape functions) are time-dependent.

The non-zero direction matrices  $\mathbf{W}_N^{Bi}$  and  $\mathbf{W}_T^{Bi}$  of beam element  $i$  (Fig. 3(c)) expressed in the global reference system, are connected with the pertinent direction matrices  $\tilde{\mathbf{W}}_N^{Bi} \in \mathbb{R}^{12,2}$  and  $\tilde{\mathbf{W}}_T^{Bi} \in \mathbb{R}^{12,1}$  expressed in the local system of each bridge element as:

$$\begin{cases} \mathbf{W}_N^{Bi} = \mathbf{R}_i^T \tilde{\mathbf{W}}_N^{Bi} \\ \mathbf{W}_T^{Bi} = \mathbf{R}_i^T \tilde{\mathbf{W}}_T^{Bi} \end{cases} \quad (15)$$

where  $\mathbf{R}_i \in \mathbb{R}^{12,12}$  is the transformation matrix accounting for the angle  $\psi_i$  between the local system (coordinate system of each beam-element) and the global coordinate system (Fig. 3(d)). It holds:

$$\mathbf{R}_i^T = \text{diag}[\mathbf{R}_{i0}^T \quad \mathbf{R}_{i0}^T \quad \mathbf{R}_{i0}^T \quad \mathbf{R}_{i0}^T], \quad \mathbf{R}_{i0}^T = \begin{bmatrix} c\psi_i & 0 & -s\psi_i \\ 0 & 1 & 0 \\ s\psi_i & 0 & c\psi_i \end{bmatrix} \quad (16)$$

where  $s$  and  $c$  are the abbreviations of the  $\sin$  and  $\cos$  function, respectively. Accounting for the geometrical relationship between the shear center of the deck section and the rail, the pertinent direction matrices  $\tilde{\mathbf{W}}_N^{Bi}$  and  $\tilde{\mathbf{W}}_T^{Bi}$  in the local system are given as:

$$\begin{aligned} \tilde{\mathbf{W}}_N^{Bi} &= [\mathbf{N}_v \quad \mathbf{N}_h \quad \mathbf{N}_\phi]^T \Gamma_v^i \\ \tilde{\mathbf{W}}_T^{Bi} &= [\mathbf{N}_v \quad \mathbf{N}_h \quad \mathbf{N}_\phi]^T \Gamma_h^i \end{aligned} \quad (17)$$

where  $\mathbf{N}_v$  (cubic),  $\mathbf{N}_h$  (cubic) and  $\mathbf{N}_\phi$  (linear) are the shape functions corresponding to the vertical flexural DOF's, horizontal flexural

DOF's and torsional DOF's [49]. Matrices  $\Gamma_v^i$  and  $\Gamma_h^i$  transfer the normal and tangential contact forces to the shear center of the bridge deck, and are given as:

$$\Gamma_v^i = \begin{bmatrix} c\phi^i & c\phi^i \\ s\phi^i & s\phi^i \\ c\phi^i e_1 + s\phi^i h & c\phi^i e_2 + s\phi^i (\Delta h + h) \end{bmatrix}, \quad (18)$$

$$\Gamma_h^i = \begin{bmatrix} -s\phi^i \\ c\phi^i \\ -s\phi^i e_2 + c\phi^i (\Delta h + h) \end{bmatrix}$$

where  $e_1$  and  $e_2$  are the lateral eccentricities (offsets).  $h$  and  $\Delta h$  are the vertical distances as in Fig. 5(a).  $\phi^i = \phi + \phi_h$  is the final tilting angle, in which,  $\phi$  is the track cant angle (Fig. 5(a)), and  $\phi_h$  is the additional rolling rotation due to the hunting motion of the wheelset (see Fig. 5(b)) [41], given in Section 2.5.

A key point of the VBI problem is the treatment of the coupling contact forces. This study adopts a macroscopic approach and hinges on the calculation of a set of equivalent contact forces per wheelset (Fig. 3(a)), similarly to [21,45]. In particular, it considers two forces per wheelset, (i.e. one per wheel) in the normal direction of contact, but only one in the tangential direction; the resultant of the contacts at the two wheels (Fig. 3(a)). The consideration of the resultant tangential force, instead of the individual tangential contact forces, is eligible by the rigid body assumption of the axle/wheelset, and, most importantly, does not over-constrain the contact problem (see e.g. [51,52]).

**Kinematic constraint:** The study assumes a continuous non-sliding contact in both directions (normal and tangential), similarly with the 'rigid' contact approach of [3]. On the acceleration level, the kinematic constraint of a sticking (no sliding) continuous contact (no separation/uplifting) is that the relative acceleration  $\ddot{\mathbf{g}}$  between the wheel and the rail is zero [48]:

$$\ddot{\mathbf{g}} = \mathbf{W}^T \ddot{\mathbf{u}} + \ddot{\mathbf{w}} = \mathbf{0} \quad (19)$$

where  $\ddot{\mathbf{w}}$  contains the additional generalized velocity terms produced during the time-differentiation and is given in the Appendix.

A limitation of the proposed approach is that it hinges on the calculation of the resultant tangential contact force (macroscopic

approach) and it ignores creep. As a result it does not allow for a realistic estimation of the individual tangential (creep) force components arising from the rolling contact between the wheel and the rail. Instead, it focuses on the calculation of the resultant tangential contact force.

From the contact kinematics (see the Appendix) and the equation of motion (10), the relative contact acceleration can be written as:

$$\ddot{\mathbf{g}} = \mathbf{W}^T \mathbf{M}(t)^{-1} \mathbf{h} + \mathbf{G}(t) \lambda + \ddot{\mathbf{w}} = \mathbf{0} \quad (20)$$

where  $\mathbf{G}(t)$  matrix is equal with  $\mathbf{G}(t) = \mathbf{W}^T \mathbf{M}(t)^{-1} \mathbf{W}$ , and its inverse  $\mathbf{G}(t)^{-1}$  represents the mass activated by the interaction;  $\mathbf{h}$  is the non-contact forces vector:

$$\mathbf{h} = \mathbf{F}(t) - \mathbf{C}\dot{\mathbf{u}} - \mathbf{K}\mathbf{u} \quad (21)$$

From Eq. (20) the contact forces vector  $\lambda$  can now be derived:

$$\lambda = -\mathbf{G}(t)^{-1} (\mathbf{W}^T \mathbf{M}(t)^{-1} \mathbf{h} + \ddot{\mathbf{w}}) \quad (22)$$

Constraint (19) with the help of Eqs. (10) and (20) yields the following equation of motion for the bridge-vehicle system:

$$\mathbf{M}(t) \ddot{\mathbf{u}}(t) + \mathbf{C}^*(t) \dot{\mathbf{u}}(t) + \mathbf{K}^*(t) \mathbf{u}(t) = \mathbf{F}^*(t) \quad (23)$$

with:

$$\begin{cases} \mathbf{C}^*(t) = [\mathbf{E} - \mathbf{W}\mathbf{G}(t)^{-1} \mathbf{W}^T \mathbf{M}(t)^{-1}] \mathbf{C} + 2v\mathbf{W}\mathbf{G}(t)^{-1} \mathbf{W}^T \\ \mathbf{K}^*(t) = [\mathbf{E} - \mathbf{W}\mathbf{G}(t)^{-1} \mathbf{W}^T \mathbf{M}(t)^{-1}] \mathbf{K} + v^2 \mathbf{W}\mathbf{G}(t)^{-1} \mathbf{W}^T \\ \mathbf{F}^*(t) = [\mathbf{E} - \mathbf{W}\mathbf{G}(t)^{-1} \mathbf{W}^T \mathbf{M}(t)^{-1}] \\ \mathbf{F}(t) - v^2 \mathbf{W}\mathbf{G}(t)^{-1} \mathbf{r}_c'' - v^2 \mathbf{W}\mathbf{G}(t)^{-1} \mathbf{y}_H'' \end{cases} \quad (24)$$

where (·)' denotes differentiation with respect to the arc length  $s^i$ , and  $\mathbf{E}$  is the identity matrix.  $\mathbf{r}_c \in \mathbb{R}^{12,1}$  is the rail elevation and alignment irregularities, as described in Section 2.4.  $\mathbf{y}_H \in \mathbb{R}^{12,1}$  is the hunting motion in the tangential direction given in Eq. (27). In the equation of motion (23), the mass matrix  $\mathbf{M}$ , the damping matrix  $\mathbf{C}^*$ , the stiffness matrix  $\mathbf{K}^*$  and the force vector  $\mathbf{F}^*$  are now time-dependent. Eq. (23) is solved using the  $\beta$ -Newmark method [50], with a time step of 0.0001 s.

#### 2.4. Simulation of rail irregularities

The study considers both elevation ( $r_{cN}$ ) and alignment ( $r_{cT}$ ) irregularities. The irregularities  $r_c$  are simulated with the spectral representation method [45] as stationary stochastic processes with suitable amplitude and wavelength:

$$r_c = \sqrt{2} \sum_{n=1}^{N_c} A_n \cos(\omega_n s^i + \alpha_n) \quad (25)$$

where  $s^i$  is the arc length;  $\omega_n = \omega_{low} + (n - 1/2)\Delta\omega$  represents a circular frequency in the interval  $[\omega_{low}, \omega_{up}]$ , with  $\omega_{low}$  and  $\omega_{up}$  being the lower and upper cut-off frequencies, respectively;  $n$  is the number of simulation points;  $\Delta\omega = (\omega_{up} - \omega_{low})/N_c$  is the frequency increment;  $N_c$  is a sufficient large number;  $\alpha_n$  denotes an independent random phase angle, uniformly distributed between the interval of  $[0, 2\pi]$ ;  $A_n = \sqrt{S(\omega_n)\Delta\omega}$  and  $S(\omega_n)$  is the rail irregularity auto-spectrum for a specific frequency of  $\omega_n$ . In this study, the German rail irregularity spectra [3] for high-speed railway are adopted:

$$\begin{aligned} \text{elevation irregularities: } S_N(\Omega) &= \frac{A_N \Omega_c^2}{(\Omega^2 + \Omega_r^2)(\Omega^2 + \Omega_c^2)} \\ \text{alignment irregularities: } S_T(\Omega) &= \frac{A_T \Omega_c^2}{(\Omega^2 + \Omega_r^2)(\Omega^2 + \Omega_c^2)} \end{aligned} \quad (26)$$

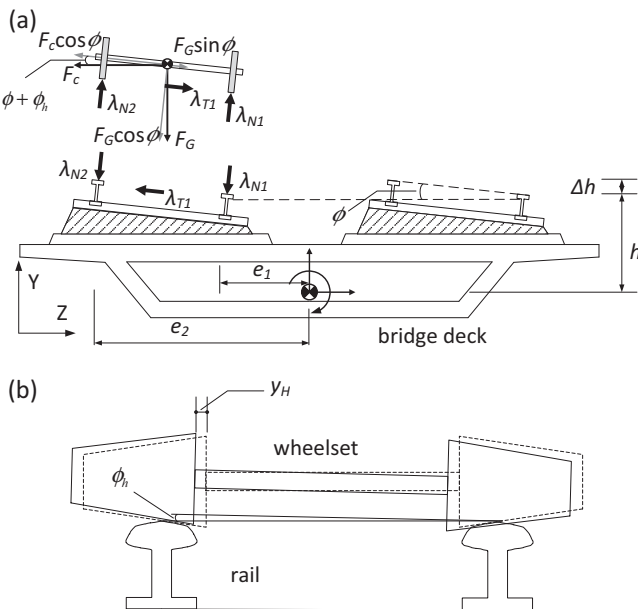


**Fig. 5.** (a) Geometrical relationship between the shear center of the bridge's deck section and the rail, and (b)  $\phi_h$  the additional rolling rotation of a wheelset due to the hunting motion.

where  $\Omega$  is the space frequency;  $A_T = 2.119 \times 10^{-7}$  m rad and  $A_N = 4.032 \times 10^{-7}$  m rad are the rail irregularity parameters;  $\Omega_c = 0.8246$  rad/m,  $\Omega_r = 0.0206$  rad/m and  $\Omega_s = 0.4380$  rad/m are the break frequencies [3].

2.5. Simulation of wheel hunting motion

The hunting motion in the tangential direction is simulated as a sinusoidal function with wave amplitude  $A_s$  and a random phase angle  $\alpha_H$  between 0 and  $2\pi$  [3]:

$$y_H = A_s \sin\left(\frac{2\pi s^i}{L_H} + \alpha_H\right) = A_s \sin\left(\frac{2\pi vt}{L_H} + \alpha_H\right) \tag{27}$$

where  $v$  is the vehicle speed;  $A_s$  is taken as 3 mm;  $L_H$  is the hunting wavelength, given by:

$$L_H = 2\pi \sqrt{\frac{l_a r_w}{\mu}} \tag{28}$$

where  $l_a = 0.75$  m is the half-gauge;  $r_w = 0.455$  m is the radius of the wheel and  $\mu$  is the effective conicity of the wheel, taken as 1/20 for a newly made wheel [3].

The lateral hunting motion causes also an additional rotation  $\phi_h$  of the wheel set due to the conicity of the wheels (Fig. 5(b)):

$$\phi_h = \frac{y_H \mu}{l_a} = \frac{A_s \sin\left(\frac{2\pi s^i}{L_H} + \alpha_H\right) \mu}{l_a} \tag{29}$$

In summary, the proposed scheme (Eqs. (23) and (24)) condenses the description of the VBI problem adopting a matrix formulation. The scheme is applicable (all matrix expressions remain unchanged) to both straight and curved bridges and accounts for rail irregularities, wheelset hunting motion, track eccentricity and different types of vehicles.

3. Comparison of the proposed scheme with existing solutions

This section compares the solutions of the proposed scheme with problems well-known in literature e.g. [42,45]. The first problem is a simple two-dimensional (2D) train model, with four DOF's, moving with constant speed ( $v = 25$  m/s) over a straight, simply supported bridge [42]. The present study integrates the complete finite element model of the (beam) bridge in the time domain, while Omenzetter [42] adopts the modal superposition method and accounts for the first three modes of vibration. The numerical results of the present study compare well (Fig. 6) with the closed-form solutions of Omenzetter [42]; the maximum relative differences are 1.16% and 1.99% for the bridge and the vehicle respectively.

Fig. 7 concerns a 3D train model with 15 identical vehicles moving with constant speed ( $v = 100$  m/s) over a straight, simply supported beam-bridge [45]. The bridge is modeled with 10 beam elements. To accommodate the multiple identical vehicles, the proposed formulation has only to augment the pertinent matrices in Eqs. (5) and (9), as shown in Eq. (14). The response midspan vertical displacements of the proposed scheme are in good agreement (Fig. 7) with the pertinent results of Yang et al. [45] (the maximum relative difference is 6.79%) considering the differences of the two mechanical models. In particular, the Yang et al. [45] study simulates the vehicle–rail–bridge interaction (as opposed to vehicle–bridge interaction) modeling also the rail as a continuous beam supported on spatially distributed spring-dashpot elements, which are then connected with the beam elements simulating the bridge.

Further, Yang et al. [45] offered analytical solutions for the response of a single-span, simply supported, curved bridge subjected to a pair of moving loads (one vertical and one horizontal).

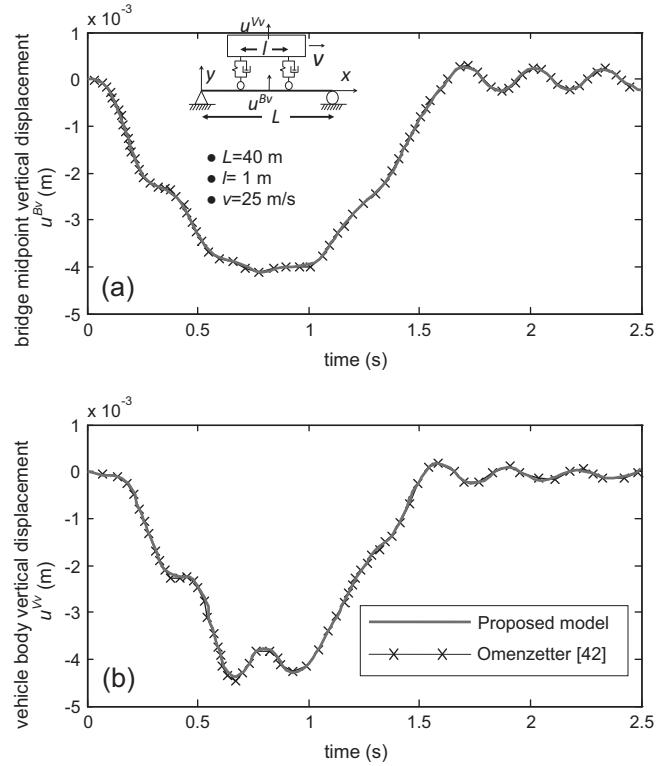


Fig. 6. (a) The midpoint vertical displacement of the bridge and (b) the vertical displacement of the vehicle-body (straight bridge, 4-DOF vehicle model).

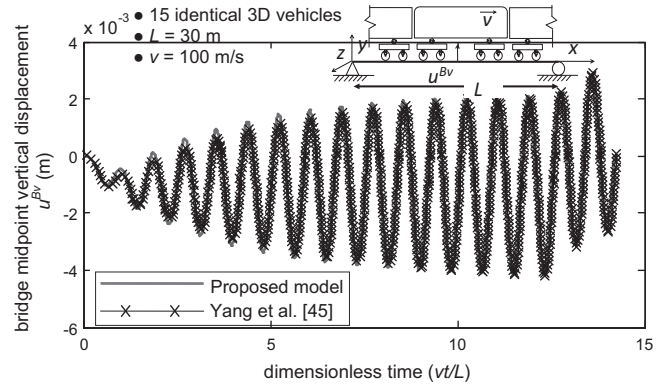
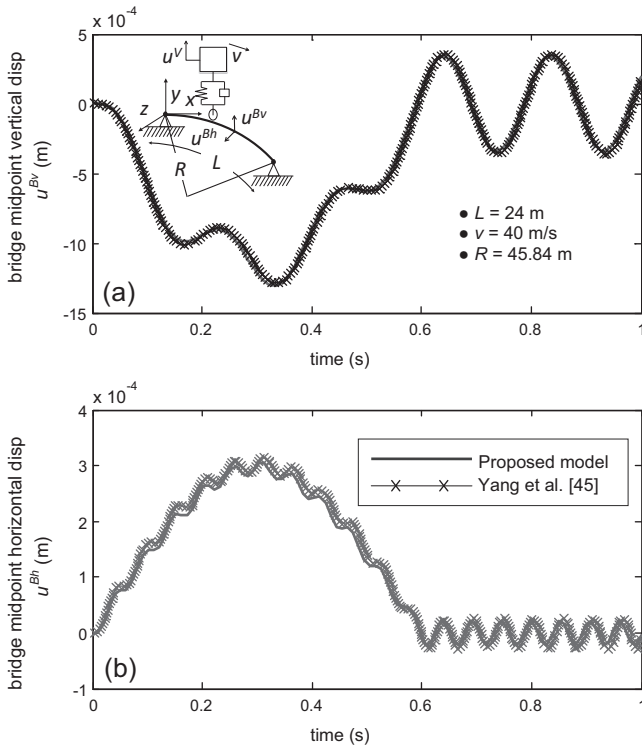


Fig. 7. The midpoint vertical displacement of the bridge; induced by the passage of 15 identical vehicles.

The proposed approach yields practically the same results (Fig. 8), for an artificially stiff (SDOF) sprung mass vehicle model (two concentrated masses connected by a spring and a dashpot) moving with the same constant speed. In particular, the maximum relative differences are 1.28% and 2.72% for the vertical and the horizontal direction respectively. Fig. 9 offers, the vertical and the horizontal, bridge midpoint, displacement spectra, of the same bridge configuration, subjected to eight pairs of moving vertical and horizontal (centrifugal) forces [45]. The VBI spectra of Fig. 9 read in dimensionless terms: the horizontal axis is expressed in dimensionless speed  $S$  [45]:

$$S = \frac{\pi v}{\omega L} \tag{30}$$

where  $v$  is the speed of the vehicle,  $L$  is the length of the bridge and  $\omega$  the corresponding natural angular frequency of the bridge. Note that, for a specific bridge (given  $L$  and  $\omega$  values) the speed param-



**Fig. 8.** The midpoint displacements of the bridge; induced by a single stiff sprung mass model (proposed model) and a moving load model [45], (a) the vertical displacement and (b) the horizontal displacement.

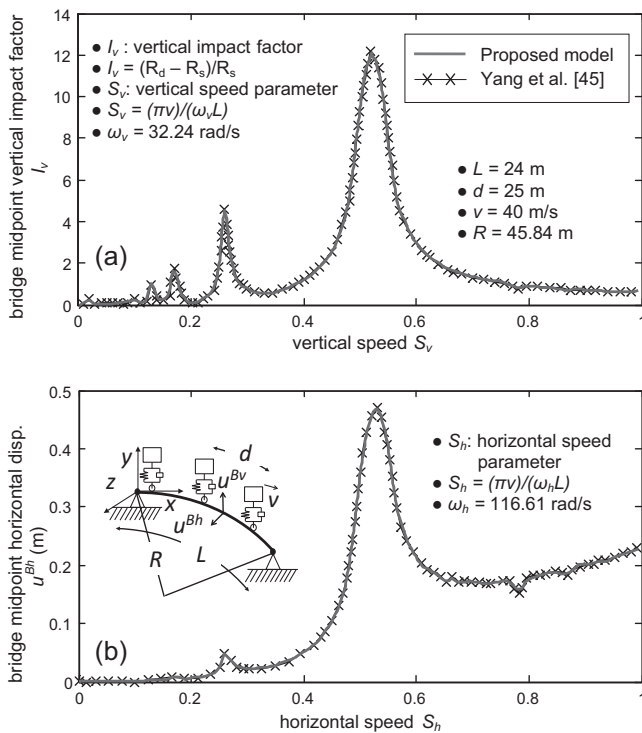


**Fig. 9.** The VBI spectra of the midpoint displacements of the bridge; induced by eight stiff sprung masses (proposed model) and eight pairs of moving loads [45]: (a) the vertical impact factor and (b) the horizontal displacement.

ter is proportional to the velocity of the vehicle. The vertical axis reads in terms of the (dimensionless) impact factor  $I$ , defined as [45]:

$$I = \frac{R_d - R_s}{R_s} \quad (31)$$

$R_d$  and  $R_s$  denote the peak dynamic and static response (e.g. of the midpoint of the bridge) respectively. Again, the proposed scheme returns the same results (Fig. 9) using eight stiff sprung mass models. The maximum relative differences are 0.82% for the vertical and 2.19% for the horizontal direction.

#### 4. Vehicle–bridge interaction: Single-span curved in-plan bridges

In curved bridges, the VBI (vehicle–bridge interaction) is not confined in the vertical direction, but triggers the response in the (horizontal) radial direction (e.g. Figs. 8 and 9), as well as, in the torsional DOF's about the longitudinal axis (of both the bridge and the vehicle). This is a distinct characteristic of the VBI dynamics in curved bridges, which in straight bridges is often neglected.

The present section focuses on the dynamic interaction between single-span, curved in-plan, railway bridges and (high-speed) trains. It builds on the work of other researchers (primarily, Xia et al. [41] and Yang et al. [45]) and brings forward the physical mechanism behind the VBI phenomenon in curved bridges, by means of a parametric analysis.

##### 4.1. Application of the proposed approach: single vehicle

Firstly, this section extends the work of Yang et al. [45], assuming a realistic 3D train vehicle (instead of pairs of loads) running on a single-span simply supported curved bridge. The characteristics of the vehicle can be found in [45]. Table 1 lists the properties of the bridge which is the same as the straight single-span, simply supported bridge of Yang et al. [45], except for the curvature, the cant angle and the horizontal eccentricities considered herein (as in Section 2.3).

In the following, when the cant angle  $\phi$  is considered in the analysis, it is assumed that it is equal with the balanced cant angle [47]:

$$\phi_{bal} = \frac{v^2}{Rg} \quad (32)$$

where  $g$  is the gravitational acceleration;  $v$  is the speed of the vehicle;  $R$  is the radius of the curved bridge.

Figs. 10 and 11 plot the vertical and radial time history displacements of the midpoint of the bridge, with and without self-excitations respectively, as well as, the pertinent radial-displacement envelopes. The envelop curves of Figs. 10 and 11 plot the peak radial displacement of the time history response analyses, for each point along the deck. The right columns of Figs. 10 and 11 present the response displacements in dimensionless terms (=dynamic

**Table 1**  
The properties of the single-span simply supported curved in-plan bridge.

Parameter	Notation	Unit	Value
Beam span	$L$	m	30
Young's modulus	$E$	GPa	28.25
Polar moment of inertia	$I_p$	$m^4$	15.65
Moment of inertia	$I_{yy}$	$m^4$	74.42
Moment of inertia	$I_{zz}$	$m^4$	7.84
Per unit length mass	$m$	t	41.74
Cross section area	$A$	$m^2$	7.73
Poisson's ratio	$\nu$	1	0.2
Eccentricity	$e_1$	m	1.88
Eccentricity	$e_2$	m	3.38
Vertical distance between the shear center of the deck-section and the lower rail	$h$	m	1.2

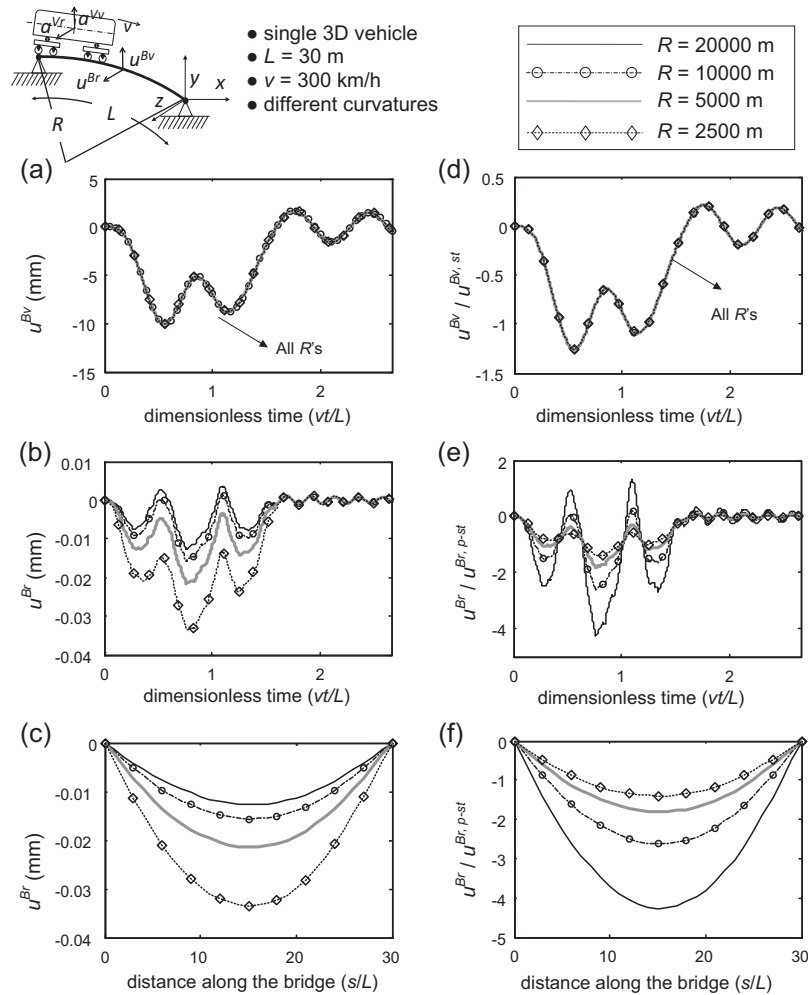


**Fig. 10.** The dynamic VBI, induced by a single vehicle on a curved single-span simply supported bridge, considering self-excitations, without a cant angle: in dimensional terms (a, b and c) and in dimensionless terms (d, e and f). Vertical (a and d) and radial (b and e) displacement time histories of the midpoint of the bridge, and the pertinent radial displacement envelopes (c and f).

response/pseudo-static response). As pseudo – “static response” we define the static response under the vehicle’s weight for the vertical direction, and under the centrifugal force  $(-m_i v^2/R)$  for the radial direction, accordingly. Note that the response along the vertical DOF’s of the bridge is unaffected (and uncoupled) by the radius of curvature, as a consequence of the small vibration theory (Figs. 10(a) and (d) and 11(a) and (d)).

The comparison of Figs. 10 and 11 brings forward the influence of the self-excitations on the radial direction of the bridge. Without the self-excitations (Fig. 11) the dimensionless midpoint radial displacements of the bridge, for different curvatures, and the pertinent envelopes, collapse to a single, unique (for a given  $L$  and  $v$ ) curve (Fig. 11(e) and (f)). As expected, as the radius decreases, the centrifugal forces increase and hence the dimensional radial displacements become higher (Figs. 10(b) and (c) and 11(b) and (c)). For a given vehicle speed, larger radii result in smaller centrifugal forces and subsequently, the self-excitations, rather than the centrifugal forces, dominate the response. When expressed in the proposed dimensionless terms, the opposite trend appears (compare Fig. 10(b), (c) and (e), (f)): the larger the radius, the higher the dimensionless radial displacement. This is true for both displacement time histories (Fig. 10(e)), as well as, displacement envelopes (Fig. 10(f)). Further, although the sign of the centrifugal forces is negative in this case, the radial displacements fluctuate between positive and negative values, due to the wheelset hunting

motion and the alignment irregularities (Fig. 10(b) and (e)). For further increase of the curvature, e.g. when  $R = 5000$  m and  $R = 2500$  m, the positive displacements disappear.

Before the train enters the bridge, it usually runs on an entry spiral curve. To investigate the effect of the entry spiral curve on the VBI, in an indirect but general way, we examine two limit cases (Fig. 12). The first corresponds to a spiral curve long enough for the train to come to an equilibrium state (in the radial direction) before entering the bridge (Fig. 12(a), (b), (e) and (f)). To simulate these conditions, we calculate the response of the vehicle running on a path of the same curvature (i.e. we apply the centrifugal and the Coriolis forces), but on a rigid ground, and we let the analysis run until the (lateral and torsional) vibration come to a deformed equilibrium configuration with zero radial acceleration. Then, the calculated displacements are used as the initial conditions of the VBI (Fig. 12(a), (b), (e) and (f)). The second limit case corresponds to the theoretical scenario that there is no entry spiral curve. In other words, the vehicle enters the curved bridge directly from a straight path and the centrifugal forces act on the vehicle suddenly; therefore, the initial radial acceleration of the vehicle is  $-v^2/R_i$  (in dimensional terms (Fig. 12(c) and (d)) or unity in dimensionless terms (Fig. 12(g) and (h))), but the initial radial displacements are zero (undeformed configuration). The pseudo-static radial acceleration  $a^{Vr, p-st}$  (e.g. Fig. 12) is defined as  $-v^2/R_i$  with the bridge radius  $R_i$ , ranging from 2500 m to 20000 m. The

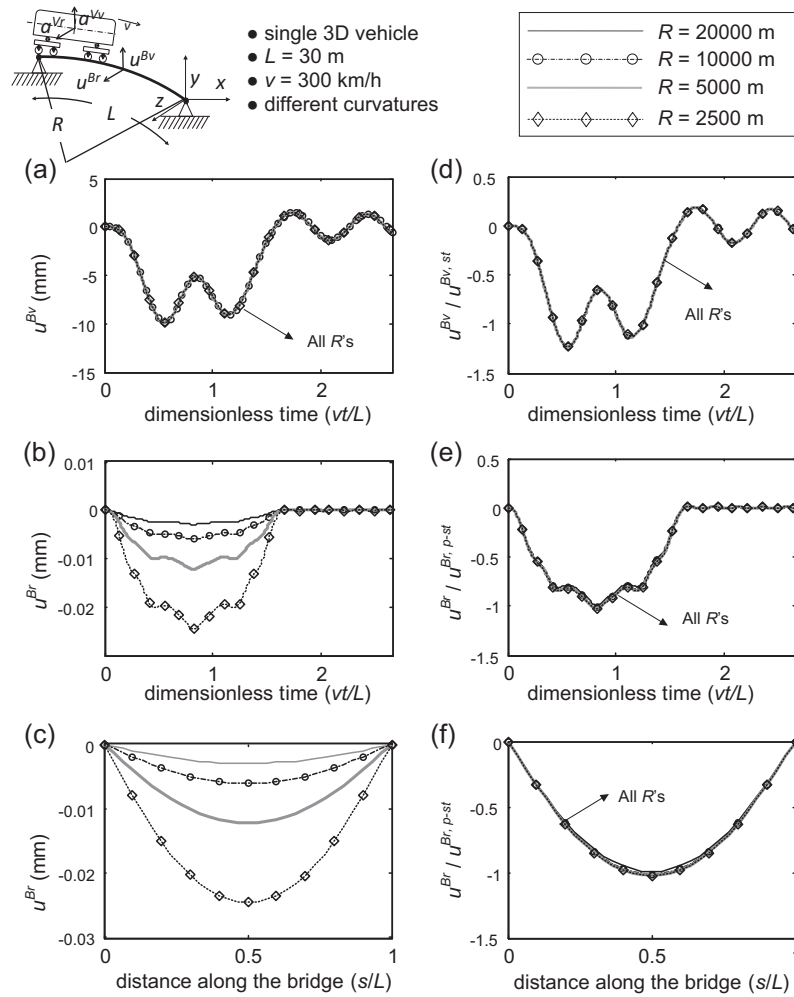


**Fig. 11.** The dynamic VBI, induced by a single vehicle on a curved single-span simply supported bridge, without self-excitations, without a cant angle: in dimensional terms (a, b and c) and in dimensionless terms (d, e and f). Vertical (a and d) and radial (b and e) displacement time histories of the midpoint of the bridge, and the pertinent radial displacement envelopes (c and f).

lateral self-excitations (the hunting motion and the alignment irregularities) trigger the fluctuation of the vehicle accelerations in the radial direction (Fig. 12(a) and (c)). Similarly to the radial response of the bridge, for a given vehicle speed, large radii result in smaller centrifugal forces and hence, the self-excitations dominate the radial accelerations of the vehicle. This is evident in the proposed dimensionless terms (Fig. 12(e) and (g)): the larger the radius the higher the dimensionless accelerations of the vehicle. On the other hand, when the self-excitations are neglected, the dimensionless radial accelerations, for different radii, all start from unity (Fig. 12(h)).

Recall that the riding comfort of the vehicle can be assessed by the accelerations of the car-body, and that it is an issue of great concern, especially for high-speed trains [45]. According to the Chinese high speed railway code [53], the vertical and lateral vehicle accelerations should be smaller than 0.13 g and 0.10 g, respectively. Fig. 12(c) and (d) shows that these limits can be insufficient in the extreme (theoretical) case where the train instantly changes from a straight to curved path, when it enters the bridge.

Two important indices which evaluate the safety of a train vehicle during VBI [53] are: (i) the *derail factor* defined as the ratio of tangential contact force  $\lambda_{Ti}$  and the normal contact force  $\lambda_{Ni}$  acting on the same wheel,

$$\text{Derail factor} = \frac{\lambda_{Ti}}{\lambda_{Ni}} \quad (33)$$

and (ii) the *offloading factor* defined as the absolute difference of the normal forces divided by the sum of the normal forces on the two wheels of the same wheelset:

$$\text{Offloading factor} = \frac{|\lambda_{Nli} - \lambda_{Nri}|}{\lambda_{Nli} + \lambda_{Nri}} \quad (34)$$

where  $\lambda_{Nli}$  and  $\lambda_{Nri}$  are the normal contact forces on left and right side wheel of the same wheelset. As a reference, according to the Chinese code [53], the allowable value for the derail factor and the offloading factor are 0.8 and 0.6, respectively. Recall, that due to the limitations of the present analysis (Section 2), the derail factor values of Figs. 13 and 14 are not based on the exact (realistic) values of the tangential contact forces. Instead, the tangential contact force is taken as half of the resultant value calculated as explained in Section 2. The same is true for Fig. 17 later on.

Figs. 13–16 display the time history of the derail factor and the offload factor, for the wheel with the smallest normal contact force (the first inner wheel with respect to the curve), when the vehicle speed is 300 km/h. Without a cant angle, the derail factor exceeds marginally the threshold of [53] when  $R$  is 5000 m (Fig. 13), and the offloading factor is beyond the requirement of [53] for  $R < 5000$  m (Fig. 15). This observation is in agreement with the minimum allowable radius of curvature for HSR bridges (5000 m according to [53]). When a balanced cant angle is used, both the

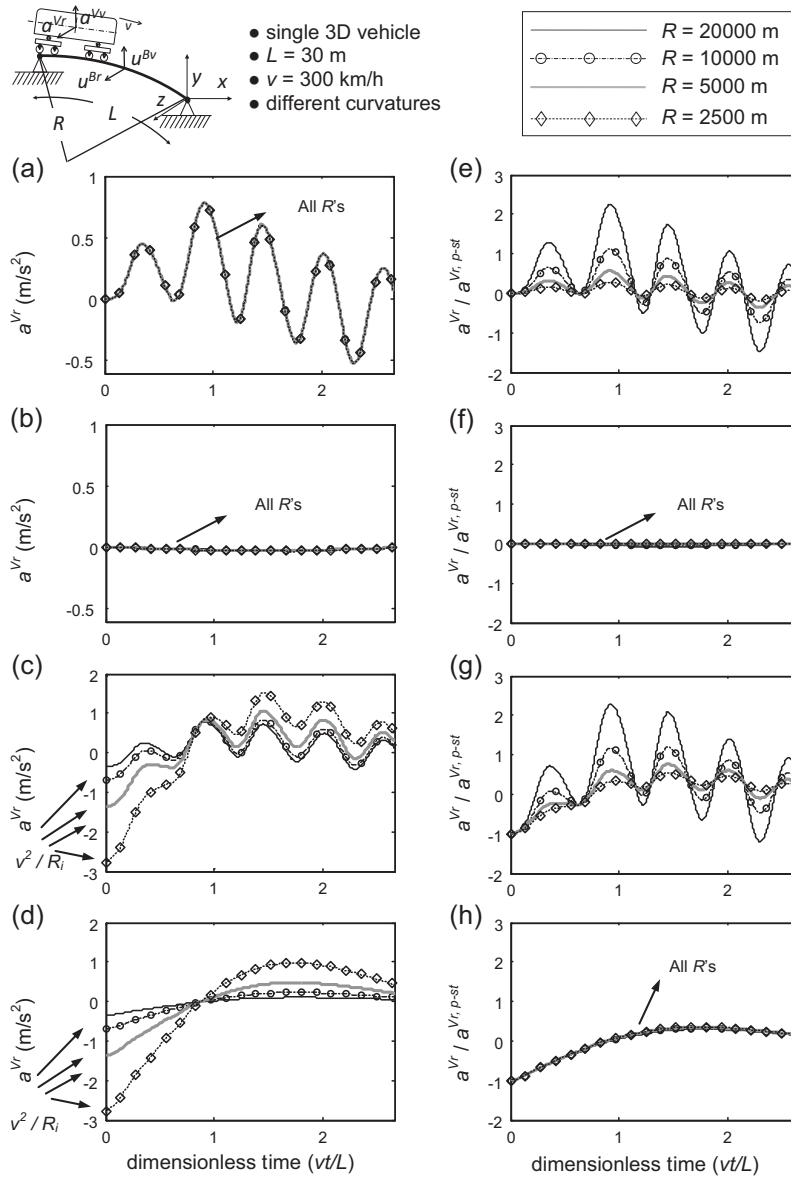


**Fig. 12.** Radial accelerations of the vehicle, induced by a single vehicle on a curved single-span simply supported bridge, without a cant angle: (a, b, e and f) considering an entry spiral curve, (c, d, g and h) without an entry spiral curve; (a, c, e and g) considering self-excitations, (b, d, f and h) without self-excitations; (a, b, c and d) are given in dimensional terms, (e, f, g and h) in dimensionless terms.

derail factor and offload factor satisfy the requirements of [53] for all curvatures (Figs. 14 and 16). As expected, the proper use of the cant angle counterbalances the lateral effect of the centrifugal forces, and increases the safety of the vehicle. The self-excitations (irregularities and hunting motion) increase both the derail factor and the offload factor, without which, the derail factor and the offload factor time history collapse to a straight line (from Figs. 13–16).

Fig. 17 gives insight into the variation of the (dimensionless) normal and tangential contact forces of the first inner wheel (with respect to the curved path). The dimensionless normal force is defined as the ratio of the normal contact force and the static weight corresponding to a specific wheel (i.e. one-eighth of the sum of the gravity forces of vehicle car body, two bogies and four wheelsets). The dimensionless tangential force is defined as the ratio of the tangential contact force and the pseudo-static centrifugal force on a specific wheel (i.e. one-eighth of the total centrifugal force of vehicle).

For a balanced cant angle, the normal contact forces are the same for all radii (Fig. 17(a)). Without a cant angle, the normal contact forces decrease with the decrease of the radii (Fig. 17(b)–(e)), for both scenarios: with (gray solid line) and without (chain dotted line) rail irregularities. This is due to the higher centrifugal forces creating higher overturning moments on the vehicle, which subsequently result in lower normal contact forces of the inner (with respect to the curve) wheel. The same trend can be seen for the tangential forces due to the lateral self-excitations (Fig. 17(f)–(i) and (j)–(m)), since for large radius, the lateral amplification effect of the hunting motion and the alignment irregularities are dominating the response. Further, for a balanced cant angle and without lateral self-excitations (third column of Fig. 17), the dimensionless tangential force is practically zero. However, without a cant angle (fourth column of Fig. 17) and without the lateral self-excitations the dimensionless tangential contact forces are equal to unity.

Fig. 18 presents, in the proposed dimensionless terms, the mid-point displacements of the bridge, and the accelerations of the

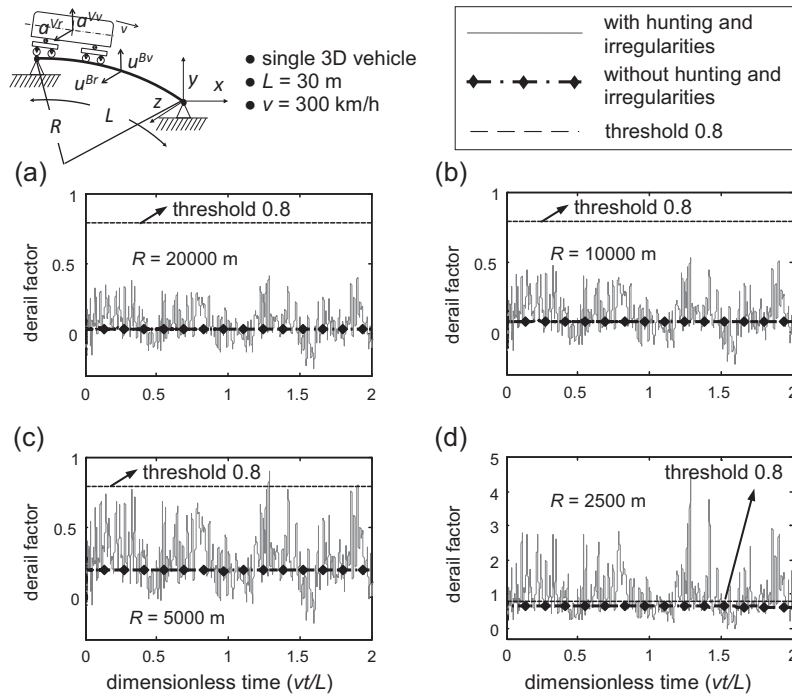


**Fig. 13.** The time history of the derail factor for first inner wheel of the vehicle; induced by a single vehicle on a curved single-span simply supported bridge, without a cant angle.

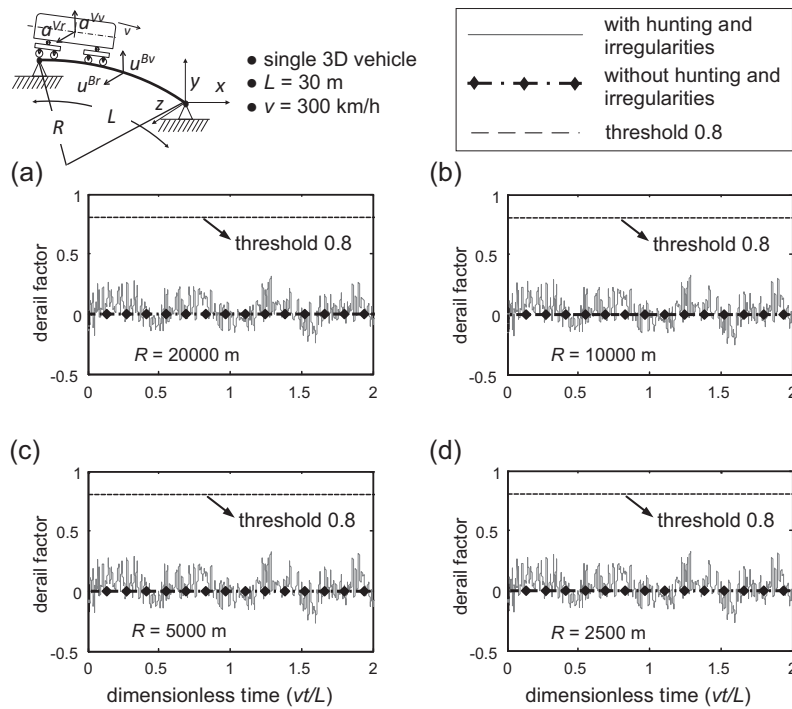


**Fig. 14.** The time history of the derail factor for the first inner wheel of the vehicle; induced by a single vehicle on a curved single-span simply supported bridge, with a cant angle.

vehicle’s car body, for speeds ranging from 100 km/h to 300 km/h. The profile of the vertical midpoint displacements of the bridge is very different depending on the speed of the vehicle (Fig. 18(a)). The dynamic fluctuation of the vertical displacement is more intense as the speed increases (Fig. 18(b)). On the contrary, the dynamic amplification in the radial direction is less intense for higher speeds (Fig. 18(d) and (e)). Recall that for a given radius of curvature  $R$ , the centrifugal force increases with the increase

of the speed of the vehicle. Hence, at low speeds, it is the hunting motion and the alignment irregularities that govern the lateral stability of the bridge and the vehicle, while at higher speeds, the lateral stability is affected mostly by the centrifugal forces and the Coriolis forces. Consequently, high speed results in larger dimensionless vertical accelerations of the vehicle (Fig. 18(c)), but smaller dimensionless radial accelerations (Fig. 18(f)).

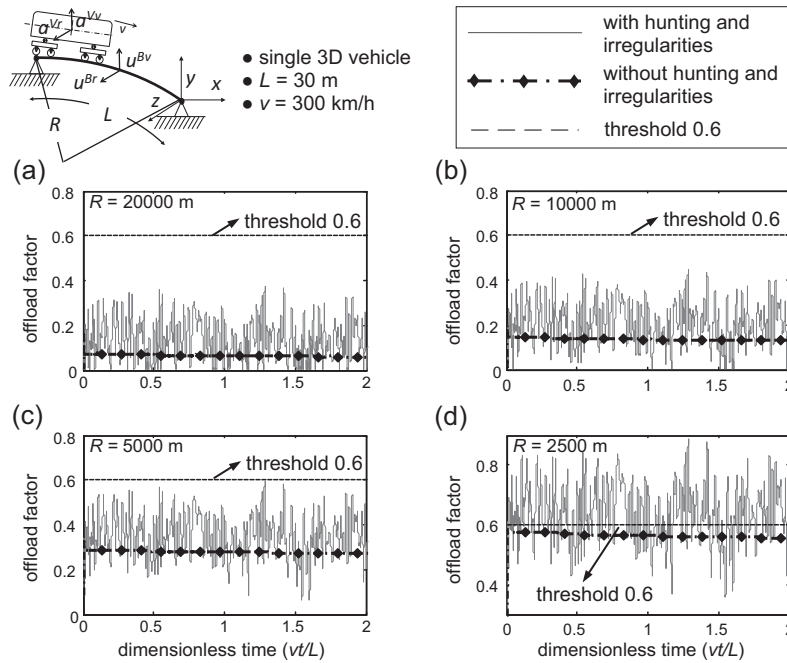


Fig. 15. The time history of the offload factor for the first inner wheel of the vehicle; induced by a single vehicle on a curved single-span simply supported bridge, without a cant angle.

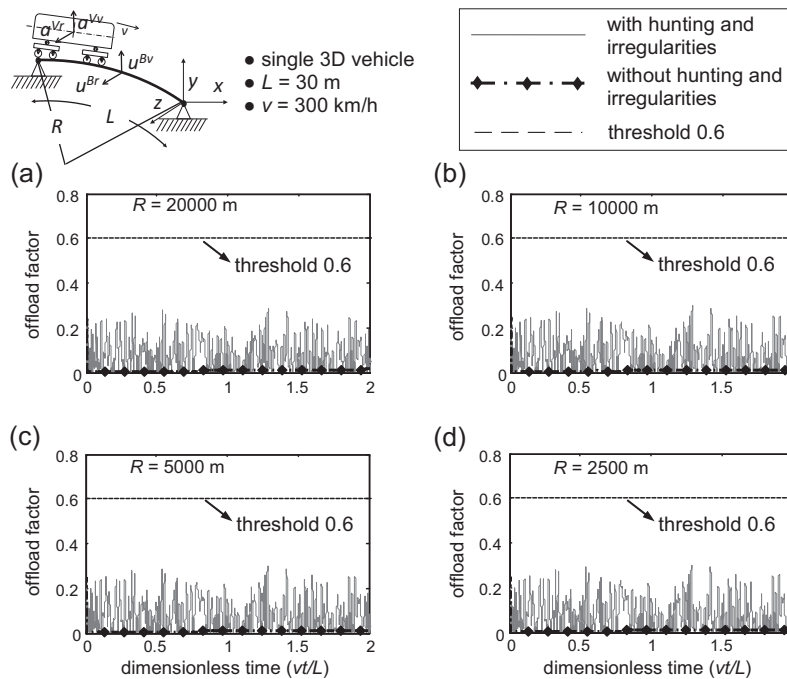
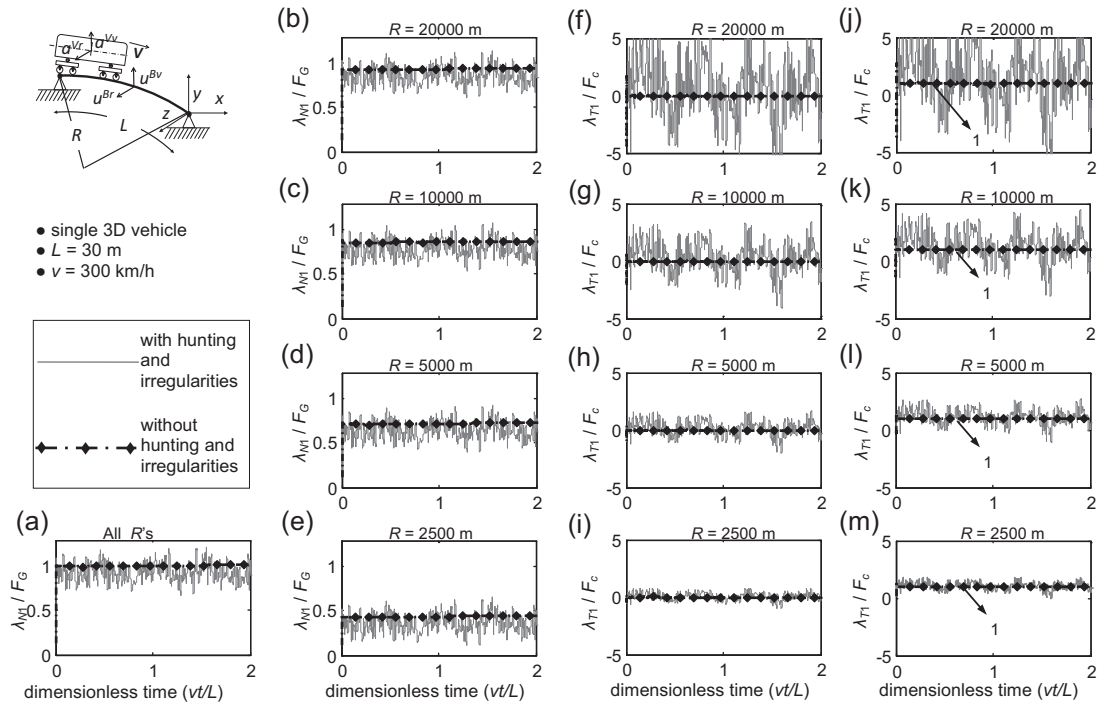


Fig. 16. The time history of the offload factor for the first inner wheel of the vehicle; induced by a single vehicle on a curved single-span simply supported bridge, with a cant angle.

4.2. Application of the proposed approach: ten identical vehicles

This section considers ten identical vehicles passing over the same bridge of Fig. 18. Fig. 19 plots the dimensionless midpoint displacements of the bridge and the accelerations of the car body of the first vehicle, in the vertical and radial directions. Unlike the single vehicle case, the repetitive loading of the multiple train vehicles, creates conditions of steady state response. Again, for low speeds, the lateral self-excitations are the main source of excitation

of the radial displacement of the bridge (Fig. 19(d) and (e)) and the radial acceleration of the vehicle (Fig. 19(f)), while the centrifugal forces and the Coriolis forces become secondary. Characteristically, the amplification of the radial acceleration of the vehicle is in the order of 2 for  $v = 100$  km/h (Fig. 19(f)). As the vehicle speed increases though, the lateral dynamics of the vehicle–bridge system is governed by the increasing centrifugal forces and the Coriolis forces. As a result, for  $v = 200$  km/h and  $v = 300$  km/h, the peak dynamic amplification of the radial acceleration is as low as 1.



**Fig. 17.** The dimensionless normal and tangential contact force time history for the first inner wheel of the vehicle; first and third column: with a cant angle; second and fourth column: without a cant angle; (a–e) normal contact forces, (f–m) tangential contact forces.

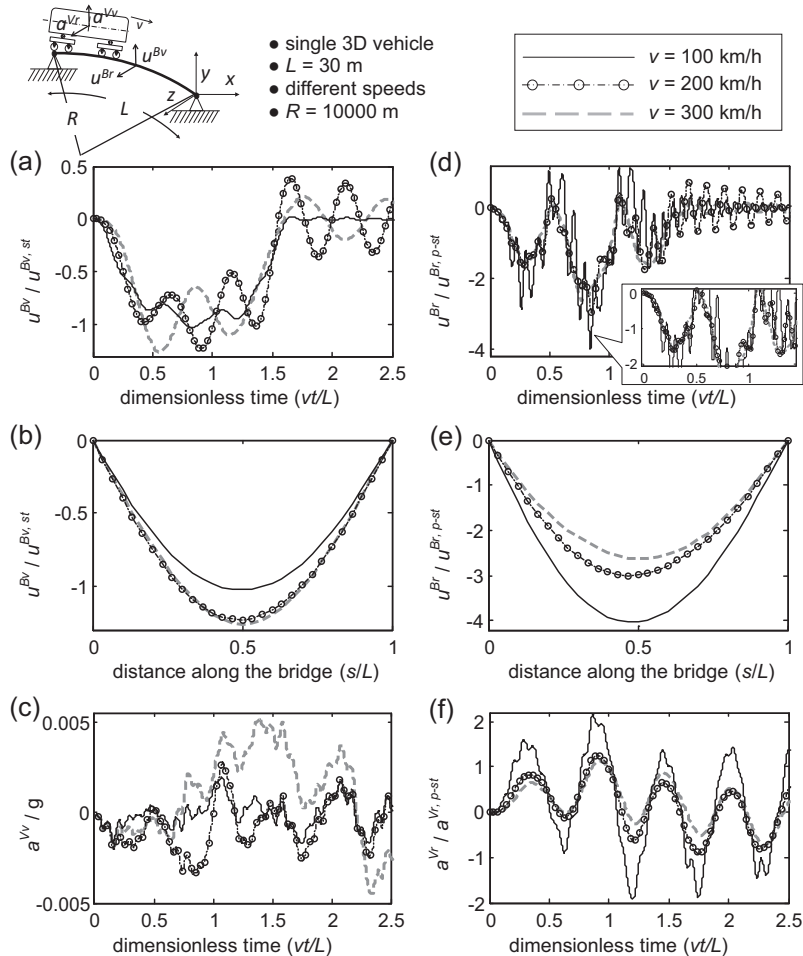


**Fig. 18.** The dimensionless dynamic VBI, induced by a single vehicle on a curved single-span simply supported bridge: the vertical direction (a–c) and the radial direction (d–f). The displacement time histories of the midpoint of the bridge (a and d), the pertinent envelopes (b and e), and the accelerations of the vehicle (c and f).

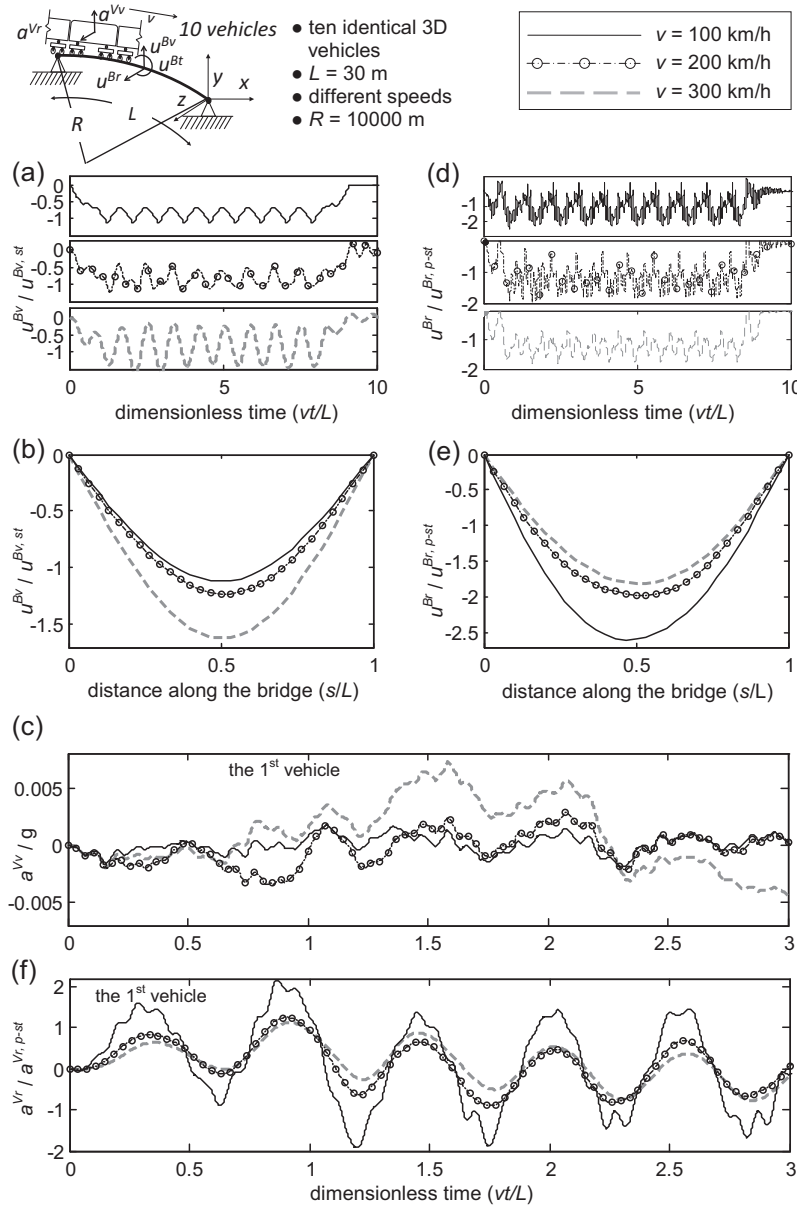


**Fig. 19.** The dimensionless dynamic VBI, induced by ten identical vehicles on a curved single-span simply supported bridge: the vertical direction (a–c) and the radial direction (d–f). The displacement time histories of the midpoint of the bridge (a and d), the pertinent envelopes (b and e), and the accelerations of the vehicle (c and f).

**5. Vehicle–bridge interaction: Multi-span curved in-plan bridges**

This section presents a pilot VBI analysis for a continuous multi-span curved bridge which is the most common structural configuration for the existing curved bridges [2]. The structural configuration examined resembles the geometry and the properties of the bridge of Fig. 2, though the radius of curvature is varied from 2500 m to 20,000 m to account for the characteristics of a HSR line. As a reference, the minimum allowed radius of curvature, for a HSR according to the Chinese standards, is 5000 m, while the recommended value is 6000–8000 m when the operational speed is 200–300 km/h [53]. It is assumed that the vertical displacements at the top of the piers are fully restrained (pinned supports). In the horizontal plane, elastic springs (with stiffness  $k = 1 \times 10^8$  N/m) are judiciously used in both directions to account for the reduced stiffness of the pier-foundation system

due to the soil-structure interaction, reported in [54]. The analysis includes the effect of self-exactions (the elevation and alignment irregularities and the wheelset hunting motion) and the eccentricity of the vehicle with respect to the shear center. It is assumed there is no cant angle and four different radii are considered. Before it enters the bridge, the vehicle is assumingly running over a long enough transient spiral curve such that, when it enters the curved in-plan bridge it has come to an equilibrium state with zero acceleration.

Fig. 20 illustrates the radial midpoint displacements of the first, the middle (fourth) and the last span, for different curvatures, together with the corresponding radial accelerations of the vehicle. Again, the radial displacements (Fig. 20(a)–(c)) increase with the decrease of the radius of curvature in dimensional terms. But in dimensionless terms, as the radius increases, the radial response decreases (Fig. 20(e)–(g)), which is also explained due to the effect of the self-excitations for lower curvatures as in Section 4.

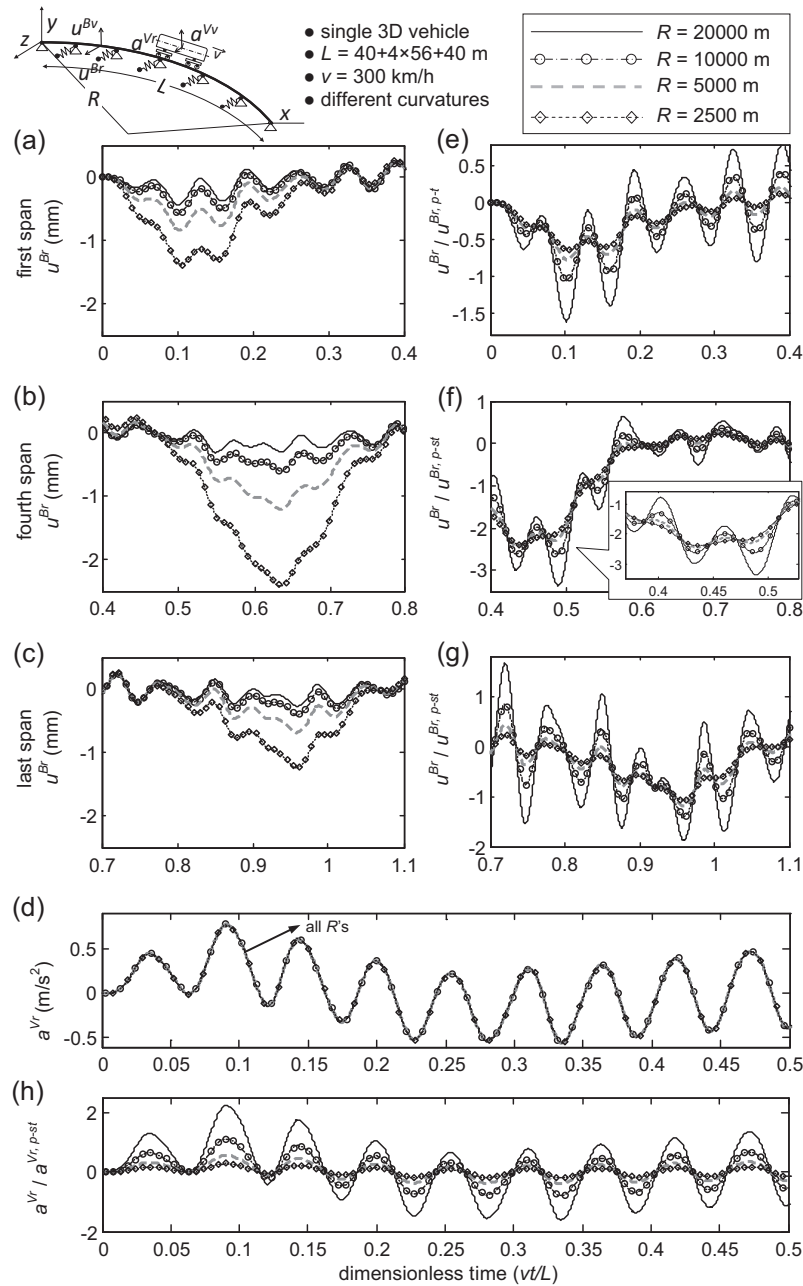


**Fig. 20.** The dynamic VBI, induced by a single vehicle on a curved multi-span bridge: in dimensional terms (a–d) and in dimensionless terms (e–h). The midpoint radial displacement time histories for the first span (a and e), the middle (fourth) span (b and f), the last span (c and g) of the bridge; the radial accelerations of the vehicle (d and h).

Figs. 21 and 22 demonstrate the effect of the vehicle's speed (from 100 km/h to 300 km/h) on the VBI response. In contrast to single-span bridges, the spans adjacent to the spans loaded by the train vehicle deflect upwards (Figs. 21 and 22). Due to the more complicated deformation patterns of multi-span continuous bridges, the influence of the vehicle's speed on the midpoint vertical displacements of the bridge is not as transparent as in the case of single-span bridges (Figs. 21(a)–(c) and 22(a)–(c)). This complexity is even more pronounced in the case of multiple vehicles crossing a multi-span curved bridge (Fig. 22). In other words, extending the analysis, and the conclusions, of the single-span to multi-span curved bridges it is not a trivial task and should be further investigated. Without a cant angle, both the derail factor and the offload factor go beyond the pertinent thresholds (0.8 and 0.6) of [54], when  $R$  is smaller than 5000 m.

## 6. Conclusions

This study proposes an original scheme for the three-dimensional analysis of the dynamic interaction between trains and curved in-plan bridges, with emphasis on high-speed railways. To this end, the proposed scheme adopts a recently proposed vehicle-dynamics formulation. In the final equations of motion, of the coupled vehicle–bridge system, all matrix/vector terms become time-dependent.

The study compares the solutions of the proposed scheme with benchmark problems from the literature. In all cases, the pertinent results are in good agreement. It further shows that the scheme accommodates easily – the matrix expressions remain unchanged – different types of bridges and vehicles, of different type, and with various degrees of freedom.

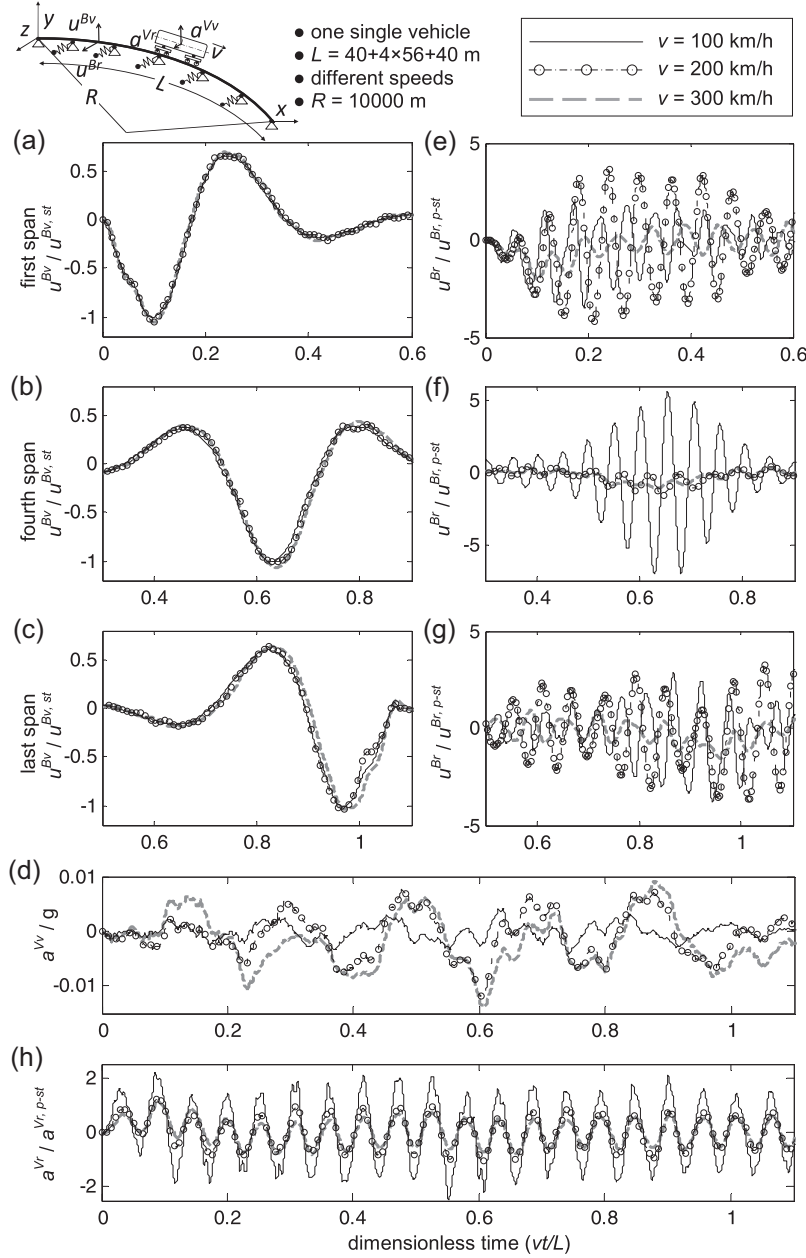


**Fig. 21.** The dimensionless dynamic VBI, induced by a single vehicle on a curved multi-span bridge: the vertical direction (a–d) and the radial direction (e–h). The midpoint displacement time histories for the first span (a and e), the middle (fourth) span (b and f), the last span (c and g) of the bridge; the radial accelerations of the vehicle (d and h).

The present paper examines both single-span and continuous multi-span curved bridges and introduces a dimensionless description that elucidates the VBI dynamics. In particular, the paper shows that the centrifugal and Coriolis forces, arising due to the curvature of the bridge/path, govern the dynamics (e.g. the dynamic amplification factor), along the radial direction, when the curvature and/or the velocity are high. On the contrary, the self-excitations (i.e. the alignment irregularities and the hunting motion) become dominant when the curvature and/or the velocity of the train vehicle are low. In contrast, within the small-deformations regime, the VBI along the vertical direction is relatively unaffected by the curvature and the self-excitations (in the radial direction).

#### Appendix A. Contact kinematics

The contact displacement (relative displacement between the wheel and the rail) is given by:

$$\mathbf{g} = [\mathbf{g}_N \quad \mathbf{g}_T]^T = \mathbf{W}^T \mathbf{u} + \mathbf{r}_c + \mathbf{y}_H = \mathbf{0} \quad (\text{A.1})$$

where  $\mathbf{r}_c$  is the vector describing the elevation  $\mathbf{r}_{cN}$  and the alignment  $\mathbf{r}_{cT}$  rail irregularities [45],

$$\mathbf{r}_c = [\mathbf{r}_{cN} \quad \mathbf{r}_{cT}]^T \quad (\text{A.2})$$

$\mathbf{y}_H$  is the wheel hunting motion in the tangential direction [3]:

After differentiation with respect to time the pertinent contact velocity becomes:

$$\dot{\mathbf{g}} = [\dot{\mathbf{g}}_N \quad \dot{\mathbf{g}}_T]^T = \frac{d}{dt} (\mathbf{W}^T \mathbf{u} + \mathbf{r}_c + \mathbf{y}_H) = \mathbf{W}^T \dot{\mathbf{u}} + \tilde{\mathbf{w}} \quad (\text{A.3})$$

with:

$$\tilde{\mathbf{w}} = v \mathbf{W}^T \mathbf{u} + v \mathbf{r}'_c + v \mathbf{y}'_H \quad (\text{A.4})$$

$$\frac{d}{dt} \mathbf{r}_c = \frac{d}{ds^i} \mathbf{r}_c \frac{ds^i}{dt} = v \mathbf{r}'_c \quad (\text{A.5})$$

$$\frac{d}{dt} \mathbf{y}_H = \frac{d}{ds^i} \mathbf{y}_H \frac{ds^i}{dt} = v \mathbf{y}'_H \quad (\text{A.6})$$

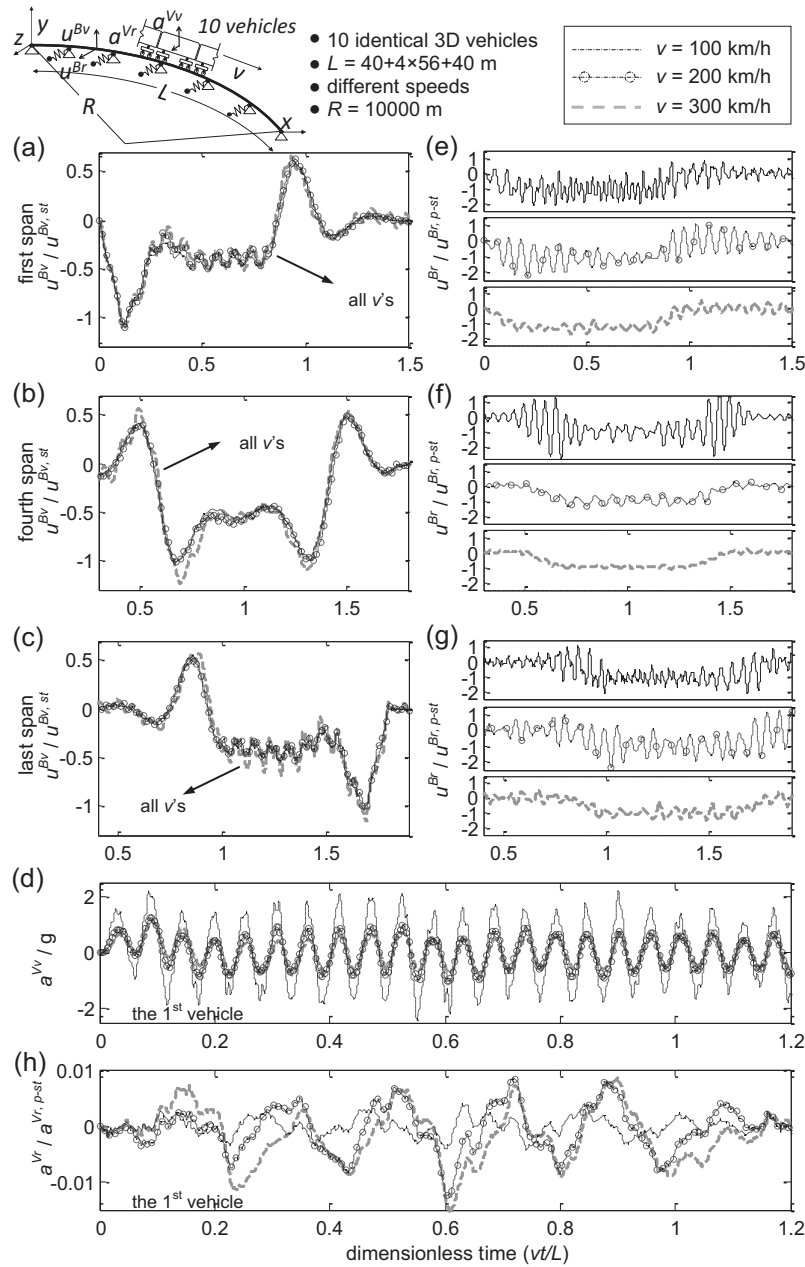


**Fig. 22.** The dimensionless dynamic VBI, induced by ten identical vehicles on a curved multi-span bridge: the vertical direction (a–d) and the radial direction (e–h). The midpoint displacement time histories for the first span (a and e), the middle (fourth) span (b and f), the last span (c and g) of the bridge; the radial accelerations of the vehicle (d and h).

$$\frac{d}{dt} \mathbf{W}_N^T = \frac{d}{dt} \begin{bmatrix} \mathbf{W}_N^V \\ -\mathbf{W}_N^B \end{bmatrix}^T = \begin{bmatrix} \mathbf{0} \\ -\frac{d}{dt} \mathbf{W}_N^B(t) \end{bmatrix}^T = \begin{bmatrix} \mathbf{0} \\ -v \mathbf{W}_N^B \end{bmatrix}^T = v \mathbf{W}_N^T$$

$$\frac{d}{dt} \mathbf{W}_T^T = \frac{d}{dt} \begin{bmatrix} \mathbf{W}_T^V \\ -\mathbf{W}_T^B \end{bmatrix}^T = \begin{bmatrix} \mathbf{0} \\ -\frac{d}{dt} \mathbf{W}_T^B(t) \end{bmatrix}^T = \begin{bmatrix} \mathbf{0} \\ -v \mathbf{W}_T^B \end{bmatrix}^T = v \mathbf{W}_T^T \quad (\text{A.7})$$

where  $(\dot{\phantom{x}})$  denotes the differentiation with respect to the arc length  $s^i$ . Similarly, for the contact acceleration after differentiation with respect to time twice, it holds:

$$\ddot{\mathbf{g}} = [\ddot{\mathbf{g}}_N \quad \ddot{\mathbf{g}}_T]^T = \frac{d^2}{dt^2} (\mathbf{W}^T \mathbf{u} + \mathbf{r}_c + \mathbf{y}_H) = \mathbf{W}^T \ddot{\mathbf{u}} + \ddot{\mathbf{w}} \quad (\text{A.8})$$

with:

$$\ddot{\mathbf{w}} = 2v \mathbf{W}^T \dot{\mathbf{u}} + v^2 \mathbf{W}^T \ddot{\mathbf{u}} + v^2 \mathbf{r}_c'' + v^2 \mathbf{y}_H'' \quad (\text{A.9})$$

## References

- [1] [http://en.wikipedia.org/wiki/File:4%2B4\\_PDL\\_network\\_in\\_China\\_\(English\\_version\).png](http://en.wikipedia.org/wiki/File:4%2B4_PDL_network_in_China_(English_version).png), 2013.
- [2] Zhang Y. Brief discussion on our country's high-speed railway bridge construction characteristics and the key technology of design. Chin Hi-tech Enterp. 2000;1:186–7 [in Chinese].
- [3] Guo WW, Xia H, Roeck DG, Liu K. Integral model for train-track-bridge interaction on the Sesia viaduct: dynamic simulation and critical assessment. Comput Struct 2012;112:205–16.
- [4] [http://www.chinadaily.com.cn/china/2011-08/23/content\\_13167866.htm](http://www.chinadaily.com.cn/china/2011-08/23/content_13167866.htm), 2013.
- [5] Timoshenko SP. On the forced vibrations of bridges. Lond Edinb Dublin Philos Mag J Sci 1922;43:1018–9.
- [6] Jeffcott HH. On the vibration of beams under the action of moving loads. Lond Edinb Dublin Philos Mag J Sci 1929;8:66–97.
- [7] Fryba L. Vibration of solids and structures under moving loads. New York: Thomas Telford; 1999.
- [8] Weaver W, Timoshenko SP, Young DH. Vibration problems in engineering. New York: John Wiley & Sons; 1990.

- [9] Wang RT. Vibration of multi-span Timoshenko beams to a moving force. *J Sound Vib* 1997;207:731–42.
- [10] Chen YH, Li CY. Dynamic response of elevated high-speed railway. *J Bridge Eng* 2000;5:124–30.
- [11] Stanišić MM, Hardin JC. On the response of beams to an arbitrary number of concentrated moving masses. *J Franklin Inst* 1969;287:115–23.
- [12] Ting EC, Genin J, Ginsberg JH. A general algorithm for moving mass problems. *J Sound Vib* 1974;33:49–58.
- [13] Sadiku S, Leipholz HHE. On the dynamics of elastic systems with moving concentrated masses. *Ingenieur Archiv* 1987;57:223–42.
- [14] Akin JE, Mofid M. Numerical solution for response of beams with moving mass. *J Struct Eng* 1989;115:120–31.
- [15] Biggs JM. Introduction to structural dynamics. McGraw-Hill College; 1964.
- [16] Au FTK, Wang JJ, Cheung YK. Impact study of cable-stayed bridge under railway traffic using various models. *J Sound Vib* 2001;240:447–65.
- [17] Pesterev AV, Yang B, Bergman LA, Tan CA. Response of elastic continuum carrying multiple moving oscillators. *J Eng Mech* 2001;127:260–5.
- [18] Pesterev AV, Bergman LA, Tan CA, Tsao TC, Yang B. On asymptotics of the solution of the moving oscillator problem. *J Sound Vib* 2003;260:519–36.
- [19] Chu KH, Garg VK, Wang TL. Impact in railway prestressed concrete bridges. *J Struct Eng* 1986;112:1036–51.
- [20] Wang TL, Garg VK, Chu KH. Railway bridge/vehicle interaction studies with new vehicle model. *J Struct Eng* 1991;117:2099–116.
- [21] Xia H, Xu Y, Chan TH. Dynamic interaction of long suspension bridges with running trains. *J Sound Vib* 2000;237:263–80.
- [22] Zhang QL, Vrouwenvelder A, Wardenier J. Numerical simulation of train-bridge interactive dynamics. *Comput Struct* 2001;79:1059–75.
- [23] Wu YS, Yang YB, Yau JD. Three-dimensional analysis of train-rail-bridge interaction problems. *Veh Syst Dyn* 2001;36:1–35.
- [24] Xu YL, Zhang N, Xia H. Vibration of coupled train and cable-stayed bridge systems in cross winds. *Eng Struct* 2004;26:1389–406.
- [25] Tanabe M, Matsumoto N, Wakui H, Sogabe M, Okuda H, Tanabe Y. A simple and efficient numerical method for dynamic interaction analysis of a high-speed train and railway structure during an earthquake. *J Comput Nonlinear Dyn* 2008;3:041002.
- [26] Zhang N, Xia H, Guo WW. Vehicle-bridge interaction analysis under high-speed trains. *J Sound Vib* 2008;309:407–25.
- [27] Dinh VN, Kim KD, Warnitchai P. Dynamic analysis of three-dimensional bridge-high-speed train interactions using a wheel-rail contact model. *Eng Struct* 2009;31:3090–106.
- [28] Zhai WM, Wang KY, Cai CB. Fundamentals of vehicle-track coupled dynamics. *Veh Syst Dyn* 2009;47:1349–76.
- [29] Dinh VN, Kim KD, Warnitchai P. Simulation procedure for vehicle-substructure dynamic interactions and wheel movements using linearized wheel-rail interfaces. *Finite Elem Anal Des* 2009;45:341–56.
- [30] Tanabe M, Wakui H, Sogabe M, Matsumoto N, Gotou K, Tanabe Y. Computational model for a high speed train running on the railway structure including derailment during an earthquake. *Adv Mater Res* 2012;579:473–82.
- [31] Antolin P, Zhang N, Goicolea JM, Xia H, Astiz MÁ, Oliva J. Consideration of nonlinear wheel-rail contact forces for dynamic vehicle-bridge interaction in high-speed railways. *J Sound Vib* 2013.
- [32] Zhang N, Xia H. Dynamic analysis of coupled vehicle-bridge system based on inter-system iteration method. *Comput Struct* 2013;114:26–34.
- [33] Yang YB, Lin BH. Vehicle-bridge interaction analysis by dynamic condensation method. *J Struct Eng* 1995;121:1636–43.
- [34] Yang YB, Yau JD. Vehicle-bridge interaction element for dynamic analysis. *J Struct Eng* 1997;123:1512–8.
- [35] Xu YL, Guo WH. Effects of bridge motion and crosswind on ride comfort of road vehicles. *J Wind Eng Ind Aerodyn* 2004;92:641–62.
- [36] Lou P, Zeng QY. Formulation of equations of motion of finite element form for vehicle-track-bridge interaction system with two types of vehicle model. *Int J Numer Methods Eng* 2005;62:435–74.
- [37] Henchi K, Fafard M, Dhatt G, Talbot M. Dynamic behaviour of multi-span beams under moving loads. *J Sound Vib* 1997;199:33–50.
- [38] Wang RT, Lin JS. Vibration of multi-span Timoshenko frames due to moving loads. *J Sound Vib* 1998;212:417–34.
- [39] Zheng DY, Cheung YK, Au FTK, Cheng YS. Vibration of multi-span non-uniform beams under moving loads by using modified beam vibration functions. *J Sound Vib* 1998;212:455–67.
- [40] Xia H, Zhang N. Dynamic analysis of railway bridge under high-speed trains. *Comput Struct* 2005;83:1891–901.
- [41] Xia H, Guo WW, Wu X, Pi YL, Bradford MA. Lateral dynamic interaction analysis of a train-girder-pier system. *J Sound Vib* 2008;318:927–42.
- [42] Omenzetter P. Interaction of a non-self-adjoint one-dimensional continuum and moving multi-degree-of-freedom oscillator. *J Sound Vib* 2012;331:833–48.
- [43] Neves SGM, Montenegro PA, Azevedo AFM, Calçada R. A direct method for analyzing the nonlinear vehicle-structure interaction. *Eng Struct* 2014;69:83–9.
- [44] [http://www.t5y.cn/inc/yeji\\_2.asp?id=118](http://www.t5y.cn/inc/yeji_2.asp?id=118), 2013.
- [45] Yang YB, Yau JD, Wu YS. Vehicle-bridge interaction dynamics. *World Scientific*; 2004.
- [46] MathWorks. *MATLAB User's Guide*. Natick, MA: The MathWorks Inc.; 1994–2012.
- [47] Shabana AA, Zaaza KE, Sugiyama H. *Railroad vehicle dynamics: a computational approach*. New York: CRC Press; 2010.
- [48] Pfeiffer F, Glocker C. *Multibody dynamics with unilateral contacts*. Springer; 2000.
- [49] Cook RD. *Concepts and applications of finite element analysis*. New York: Wiley; 2007.
- [50] Clough RW, Penzien J. *Dynamics of structures*. New York: McGraw-Hill; 2003.
- [51] Dimitrakopoulos EG. Analysis of a frictional oblique impact observed in skew bridges. *Nonlinear Dyn* 2010;60:575–95.
- [52] Dimitrakopoulos EG. Nonsmooth analysis of the impact between successive skew bridge-segments. *Nonlinear Dyn* 2013;1–18.
- [53] China's Ministry of Railways. *Code for Design of High Speed Railway*. Beijing China: China's Ministry of Railways; 2009. [in Chinese].
- [54] Ding MB, Chen XC, Wang KZ. Self-vibration characteristic test of continuous curved railway bridge by means of environment random excitation. *J Lanzhou Jiaotong University* 2008 [in Chinese].